A geochemical evaluation of cryptotephra from Montserrat, Lesser Antilles Arc

by

Mattison Hood Barickman

A Senior Honors Thesis for the Department of Earth & Ocean Sciences

Submitted in partial fulfillment of the requirements for the degree of

BACHELOR OF SCIENCE
in Geological Sciences
at
TUFTS UNIVERSITY
College of Arts & Sciences. Class of 2018

Thesis Committee:
Molly C. McCanta: Committee Chair, Associate Professor, University of Tennessee, Knoxville
Anne F. Gardulski: Undergraduate Advisor, Associate Professor, Tufts University

Tufts
Earth
and Ocean
Sciences

Special thanks go out to the National Science Foundation, whose grant #1347882 supported the research for this project.

A geochemical evaluation of cryptotephra from Montserrat, Lesser Antilles Arc

by ***Mattison Hood Barickman***

ABSTRACT

In volcanic eruptions, magmatic or phreatomagmatic fragmentation transforms the erupting magma into a gas-particle/droplet mixture that is then injected into the atmosphere as an ash plume. The material from this ash plume is then deposited on land or in the ocean as a tephra layer, an unconsolidated, fragmented material, or cryptotephra, which is a tephra layer that is invisible to the naked eye. Tephra has long been used in geochemical studies of volcanic systems to assess how the magma chambers evolve in terms of their composition and volatile content. It is particularly useful as a chronostratigraphic marker that can provide precise age dates for both ice and oceanic cores. This project explores two newly documented cryptotephra deposits from core U1396-1H-4W collected on IODP expedition 340 to the Caribbean Sea, near Montserrat. The overall particle content and composition is documented through point counting. Textural analysis via scanning electron microscopy (SEM) indicates that white glass, mineral fragments, and vesicular pumice fragments are the main constituents of these cryptotephra deposits. A geochemical evaluation of glass particles in both deposits indicates that samples range in composition from rhyolitic to dacitic. The variation in composition of glass particles in core segment 11-15 cm can be attributed to one of two processes: mixing of a more silicic and a more mafic magma in the chamber which feeds the various volcanic complexes on Montserrat, or a relatively fast ascent rate of magma through the crustal column which leads to relatively less degassing until the magma reaches the subaerial environment. The low variance in composition of glass particles in core segment 41-45 cm suggests that the magma either ascended through the conduit at a slower rate and degassed as it rose, or that the magma chamber fractionated significantly before the eruption.

Acknowledgements

This past year's work on my honors thesis has been founded on the encouragement, inspiration, and support of numerous people. First and foremost, I would like to thank my committee chair, Molly McCanta. It was in your classes that I began to feel a real passion towards the fields of geology and geochemistry. Your work as a scientist and as a professor has been and will continue to be an inspiration for me in years to come. You have allowed me to approach scientific questions from an open and creative point of view, aided me in topics that confuse me, and challenged me to hold myself and my ideas to a higher standard.

I'd also like to thank my undergraduate advisor Anne Gardulski, who has helped guide me through the many challenges that arise during one's time as a college student. Academically, you have pushed me to take classes outside of my comfort zone that have ultimately led me to have a broader and more complete perspective on geology. Professionally, you have taught me the ins and outs the scientific community, and how to conduct myself when visiting other institutions or getting interviewed. You have helped walk me through times I struggled in my classes. And, most importantly, you have kept me on schedule with this thesis. I would not be handing in a complete, polished product without your help.

Beyond this committee, several other people have been integral to the success and completion of this thesis. Neel Chatterjee, thank you so much for your help during the several microprobe sessions I had at MIT. Brian Monteleone and Kathryn Rose Pietro, thanks for teaching me about Secondary Ion Mass Spectrometry and showing me how to work the 3f. In addition, I can't thank you enough for helping me tackle the technical malfunction we experienced, and for running my samples even though I was not present. And, of course, a multitude of thanks go out to Jacob Benner; Jake, you have helped me handle 90% of the technical problems that have arisen with the SEM, microscope cameras, and lab computers, in addition to being an amazing friend and inspiration to me. You are so passionate about helping students learn geology, and I can only hope to be as good of a professor as you one day.

Jack Ridge, Andrew Kemp, and Grant Garven: on top of all the other academics I have thanked, you too have aided me in this thesis. Each of your classes has taught me to approach the broad field of geology and the interpretation of the results of this project from different points of view. Thank you all for your guidance during my time as a student at Tufts and for helping me to obtain a broad, diverse education in the geosciences.

I am also grateful for the support from my fellow undergraduates, particularly Jack Baer and Jacob Marsh, who have been on this journey with me since the beginning. I don't think that I would have had such an enjoyable time majoring in Geological Sciences without both your support and friendship. To every other geology major whose name I've failed to mention, thanks for keeping me sane and spending countless hours in the basement of Lane with me. The fun moments we've shared together are memories I will cherish for the rest of my life.

To my boyfriend Andrew, thank you for your unwavering support and love for me, even in this long semester of an across-the-world long distance relationship. I love you and will miss you dearly next year.

And last, but certainly not least, I would like to thank the "rock" in my life, my family. To my mother and father, thank you so much for teaching me the value of an education and pushing me to be the best student and the best person I can possibly be. Pursuing geosciences was never something I considered before college, but you have encouraged me to follow my heart and my gut while at Tufts, and you are the reason I am where I am today. And to my sister, you have been such a close friend for eighteen years now. It is your humor, honesty, and bold personality that encourage me to believe in myself and follow my dreams.

Table of Contents

1 | INTRODUCTION

1.1 Why study Montserrat (and its three volcanic complexes)?

Volcanic eruptions are one of the most remarkable physical processes that occur on Earth. They have the ability to shape Earth's climate, surficial processes, biosphere, and the way that humans interact with the land they live on. Active volcanoes are constantly feeding material to Earth's atmosphere and surface, and not only can they be destructive, they can also be sources of geothermal energy, ore deposits, and fertile soils. In the year 2000, approximately 500 million people were predicted to have lived in areas at risk from volcanic eruptions, 90% of whom would have lived near a volcano on a convergent margin (*US Geological Survey,* 1994). With a population explosion in many of these same regions in recent years, more intensive monitoring and studying of volcanic regions is crucial to understanding how these complex systems behave. An accurate way to predict or understand the relative frequency of volcanic eruptions still does not exist. Developing a comprehensive volcanic record, therefore, is absolutely necessary in order to be prepared for future eruptions and to understand the systems and processes specific to a certain volcano.

In December 1995, Montserrat's South Soufrière-Soufrière Hills (SS-SH) volcanic complex (Figure 1) was reactivated for the first time in several centuries. The lava-dome-forming phreatomagmatic eruption continued until March 1998. The initial eruption and resurgent pyroclastic flows (generated by subsequent lava dome collapses) ultimately destroyed the capital city of Plymouth, blanketing it in over 12 meters of ash. Landslides and lahars also decimated much of the communities surrounding the volcanic complex. Even to this day, the southern half of Montserrat is restricted to both inhabitants and tourists (*United Kingdom Foreign & Commonwealth Office,* 2018).

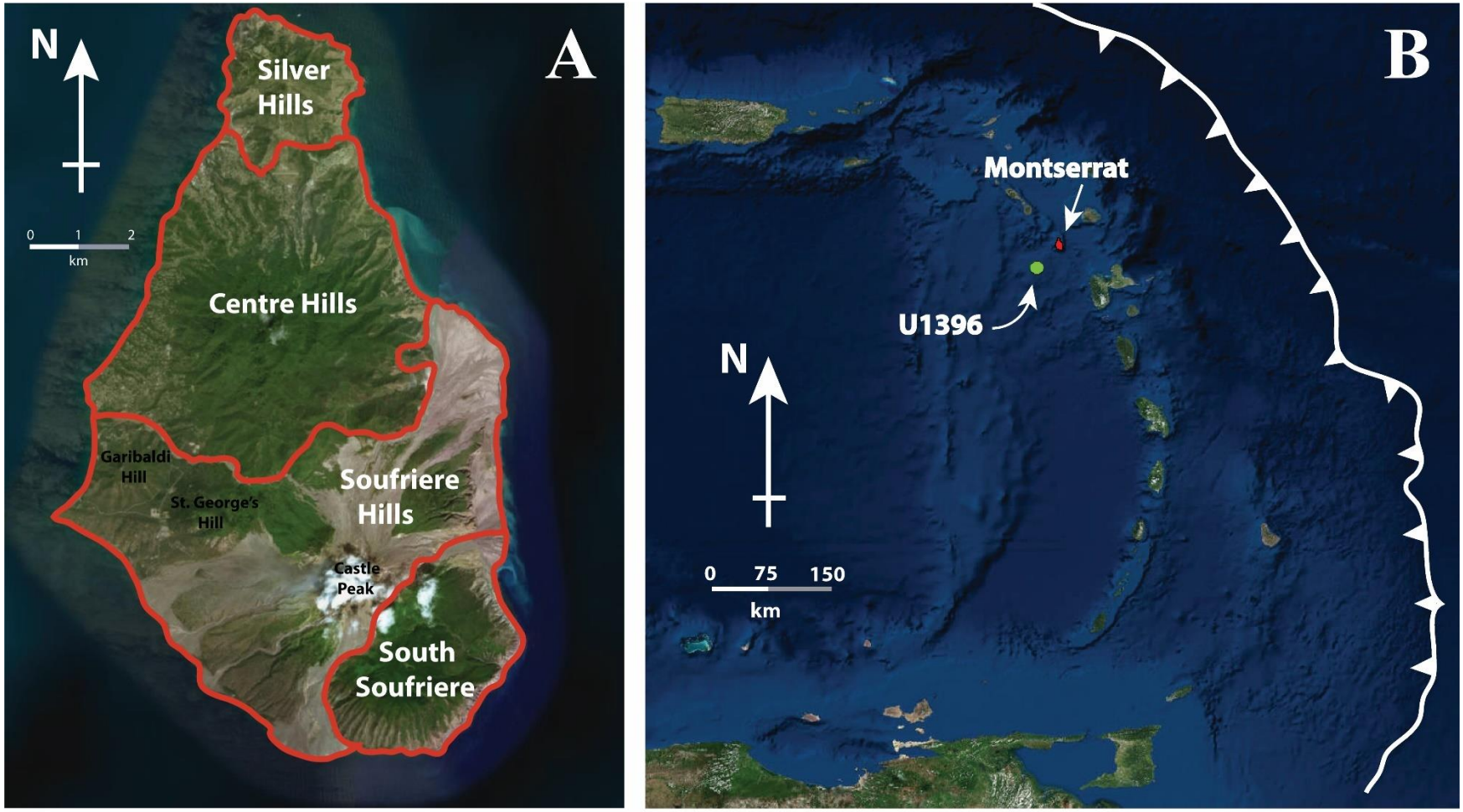

Figure 1. A. Location of Montserrat and core U1396 within the Lesser Antilles Arc and Caribbean Sea. **B.** A map detailing the island of Montserrat, adapted from Zellmer et al. (2003), including the four different volcanic regions on the island.

Explosive eruptions like this have been well-documented and studied in recent history (past 200 years). In fact, the 1995-1998 eruption of the SS-SH volcanic complex is one of the most extensively studied eruptions of all time, due to how recent and destructive it was (Rutherford et al., 1998). However, completely understanding the most recent eruptions does not provide us with the full picture of how a volcano functions or evolves, factors which are necessary to understand in order to assess how a volcano will continue to behave in the future. In order to do this, we must turn to prehistoric eruptions that may not be easily accessible in the geologic record.

Tephra is defined as unconsolidated, fragmented volcanic material of any grain size that is ejected during an explosive eruption and deposited via atmospheric fallout or pyroclastic density currents (Lowe, 2011). More than 90% of the total volume of material erupted in historic times from subaerial volcanoes is tephra. It can either be deposited on land or in the oceans. In the case of the SS-SH volcanic complex, much of its tephra would have been deposited on the ocean floor (in recent geologic history, i.e. past 200,000 years). Here, these eruptions are preserved as either thick, visible layers representing either relatively larger or proximal eruptions, or thin layers representing relatively smaller or distant eruptions. These thin layers are typically undetectable to the naked eye and can only be identified using spectroscopic or magnetic methods; they are commonly referred to as cryptotephra (Lowe, 2011). This study will focus on these cryptotephra layers from oceanic drillcores collected off the coast of Montserrat and how they can add to our understanding of Montserrat's volcanic history and the evolution of its magma storage region. Ideally, the conclusions made in this study may also be extended to the larger scale of the whole Lesser Antilles Arc, as volcanic activity throughout this system is linked to similar subduction processes.

1.2 Tephra, Cryptotephra, Cryptotephra Identification

As mentioned earlier, tephra is as an unconsolidated, fragmented material that is ejected during an explosive eruption and deposited by atmospheric fallout or a pyroclastic flow (Lowe, 2011). Tephra can comprise glass shards, crystal fragments, and volcaniclastics that are made of fragmented rocks and lava (Lowe, 2011; Cassidy et al., 2014). Tephra units that are thinly dispersed and invisible to the naked eye are better known as cryptotephra (Le Friant et al., 2008; Lowe, 2011; Cassidy et al. 2014). Tephra can be used as isochrons to connect or correlate sequences and to transfer relative or numerical ages to such sequences where the tephra have been dated (Lowe, 2011). Not only are tephra layers useful for age-dating stratigraphic sequences; their physical and geochemical properties can be documented through several different techniques (Lowe, 2011). These properties can allow for correlation across wide areas to serve as precise datums for archaeological, environmental, and geological events, and also for studying the geochemical evolution, eruptive history, and source of the volcanic systems with which they are associated. In order to do this, tephra deposits close to a volcanic center must be carefully recorded and comprehensively documented. This can be difficult for subaerially deposited tephra sequences, as they are often obscured by burial and/or vegetation and may be subject to extensive erosion and chemical weathering (McCanta et al. 2015). However, submarine tephra deposits proximal to a volcanic center are usually well-preserved, as they are isolated by marine pelagic deposits (thereby keeping them in place and fairly pristine).

The process of characterizing, correlating, and dating tephra layers in a stratigraphic sequence is called tephrochronology (Lowe, 2011). Tephrochronology can be used to understand the evolution of a volcano's eruptive frequency, explosivity, eruptive style, and geochemistry over time as long as deposition is continuous, deposits are correctly identified as primary or

secondary, and the recorded tephra sequence is complete (Lowe, 2011). However, interpretations from tephrochronology can be hindered due to the fact that minor or distal eruptions result in tephra layers so fine and dispersed that they are invisible to the naked eye. These fine, "invisible" tephra units are the units referred to as cryptotephra throughout the rest of this study (Le Friant et al., 2008; Lowe, 2011; Cassidy et al. 2014). The exact definition of cryptotephra is still ambiguous and some have attempted to narrow it according to grain size and lithology of volcanic materials, although, it is generally accepted that multiple depositional processes (both primary and secondary [i.e. remobilized debris flows, lahars, turbidity currents, etc.]) can lead to the formation of stratigraphic cryptotephra layers. It is this variety of deposition processes that creates ambiguity in the definition (Le Friant et al., 2008; Cassidy et al., 2014).

Until recently, the rapid identification of cryptotephra has been hindered, due to the fact that deposits are invisible to the naked eye. A recent study incorporating a former Senior Honors Thesis at Tufts University by Elizabeth Fisher (2015) evaluated reflectance spectroscopy as a method of rapid cryptotephra identification. The author collected VSWIR (Visual Short-Wave Infrared) [0.4-2.5 μm] reflectance spectra at 0.5 cm down-core resolution using an ASD Fieldspec© spectrometer and identified potential cryptotephra layers using spectral summary parameters sensitive to iron content (0.95 μm integrated band depth) and clay minerals (2.202 μm band depth). Fisher was able to determine spectral signatures indicative of tephra and correlate cryptotephra layers with increased percentages of pumice and juvenile/angular volcanic materials likely emplaced by explosive eruptions (Fisher, 2015). As that study was successful in identifying multiple cryptotephra layers *in situ,* it paved the way for future studies on the geochemistry of cryptotephra and how it evolves over different eruptions for volcanic systems.

1.3 Analyzing Cryptotephra Records in Island Arc Systems

Primary cryptotephra deposits produced by either fallout from explosive eruptions or pyroclastic density currents are useful for generating an eruptive history of the volcano with which they are associated (Cassidy et al., 2014). Cryptotephra emplaced by primary fallout may result from distal, explosive eruptions (e.g., Plinean, Supervolcanic, etc.) that shoot ash high into the atmosphere where it is widely dispersed; it may also be emplaced by small, proximal eruptions that release only a small amount of ash (Cassidy et al., 2014). If a cryptotephra unit is deposited from a pyroclastic density current, it might represent ash at the very edges of the flow.

Cryptotephra can also be emplaced by secondary depositional processes, such as the reworking of deposits via bioturbation or erosion by seafloor currents (Cassidy et al., 2014). Other remobilization processes include submarine flank collapses, subaerial landslides, lahars, slope collapses, and turbidity currents. Secondary deposits are less useful for dating because primary deposits can be reworked thousands of years after their initial deposition (Cassidy et al., 2014). When the reworked cryptotephra deposits are redeposited, the dates yielded from analyses of their various particles are representative of an eruption that occurred many years before their secondary deposition. In order to determine whether or not a deposit is secondary, one must identify certain sedimentary structures associated with the deposits (such as evidence for turbidity flows, biogeneous material, etc.).

Tephrochronological studies rely upon precise and accurate geochemical quantitation. Marine cryptotephra studies can provide a lengthier and more accurate window into the volcanic history of island arc volcanoes than those provided by land-based data. In contrast, the subaerial tephra (and cryptotephra) deposits are either buried, chemically weathered, or eroded significantly by surficial processes. Whereas, tephra sequences preserved in lake sediments or marine sediments at medial or distal sites may provide a more comprehensive and accurately

assessable record of eruptive history that is less easily corrupted by erosion and/or weathering. In addition, these stratigraphic sequences can enable the interfingering and superpositioning of eruptive material from any volcanic complex that is located near a marine or lake environment (Lesser Antilles Arc, Aleutian Island Arc, Indonesian Island Arc, etc.), which allows for the precise dating of different eruptive periods and understanding of the relation between volcanic deposits and associated sedimentary layers.

In addition to understanding the volcanic history of Montserrat and surrounding volcanic centers, major, minor, and trace element data from glass particles and minerals can be used for geochemical fingerprinting. This is because the composition of cryptotephra particles can be affected as a singular magma chamber evolves, or if different cryptotephra layers are generated from different volcanic centers. Geochemical characteristics of all magma chambers and volcanic systems are best preserved in glass particles, representative of quenched melts. Glass is an amorphous solid with a non-crystalline internal structure comprising loosely linked SiO_4 tetrahedra that can fit various cations (e.g., Ca, Na, K, Fe, Mg) into the intramolecular space (Lowe, 2011). Due to the unique properties of glass, SEM, EPMA, and SIMS can reveal characteristics about eruptions and pre-eruptive conditions that mineral analyses cannot. For example, major element analyses of glass can enable volcanic provenance to be identified and can allow us to investigate how a magma chamber is evolving. Or, they can help us geochemically characterize an entire succession of tephra/cryptotephra deposits within a core, whether or not they are generated by a wide range of eruptive styles (Lowe, 2011). Even if deposits are in short stratigraphic succession and show no evidence of hiatuses, different eruptions can be determined based on their geochemistry.

In addition to glass, the composition of minerals in cryptotephra layers can be useful in studying the eruptive conditions and crystallization conditions at depth (P, T, f_{O_2}). The precise chemical compositions of plagioclase, pyroxene, amphibole, olivine, spinels, and Fe-Ti oxides can be used to source volcanoes and study the crystallization and ascent conditions within the crustal column (Lowe, 2011). Using cryptotephra to study short-term evolution of the upper continental crust is a relatively new technique and allows us to explore how volcanoes and the magma chambers that feed them have evolved.

1.4 Geologic History & Tectonic Setting

The geologic history of the Lesser Antilles Arc begins with the formation of the Atlantic Basin, approximately 175 million years ago during the Jurassic when Pangea began to separate (Garmon et al., 2017). 25 million years later, rifting began between the supercontinents of Gondwana and Laurasia centered on the Mid-Atlantic Ridge, leading to decompression melting in the upper mantle to produce magma flows that cooled to form new oceanic crust. Then, in the Late Cretaceous (approximately 80 million years ago), the Caribbean Plate began to subduct under the South American Plate, leading to island arc volcanism 40 million years ago. Interestingly, however, the primarily evolved, continental South American Plate subducts underneath the more primitive, oceanic crust of the Caribbean Plate at certain locations, such as Northern Venezuela. This is due to steady pile-up of pelagic sediment on the South American Plate, which over time made it heavier and denser than the Caribbean Plate, effectively leading to the formation and evolution of the Lesser Antilles subduction zone and associated island arc (Garmon et al., 2017). The evolution of the Lesser Antilles Arc from the Pliocene to the present day, using data from Garmon et al. (2017), is presented in Figure 2.

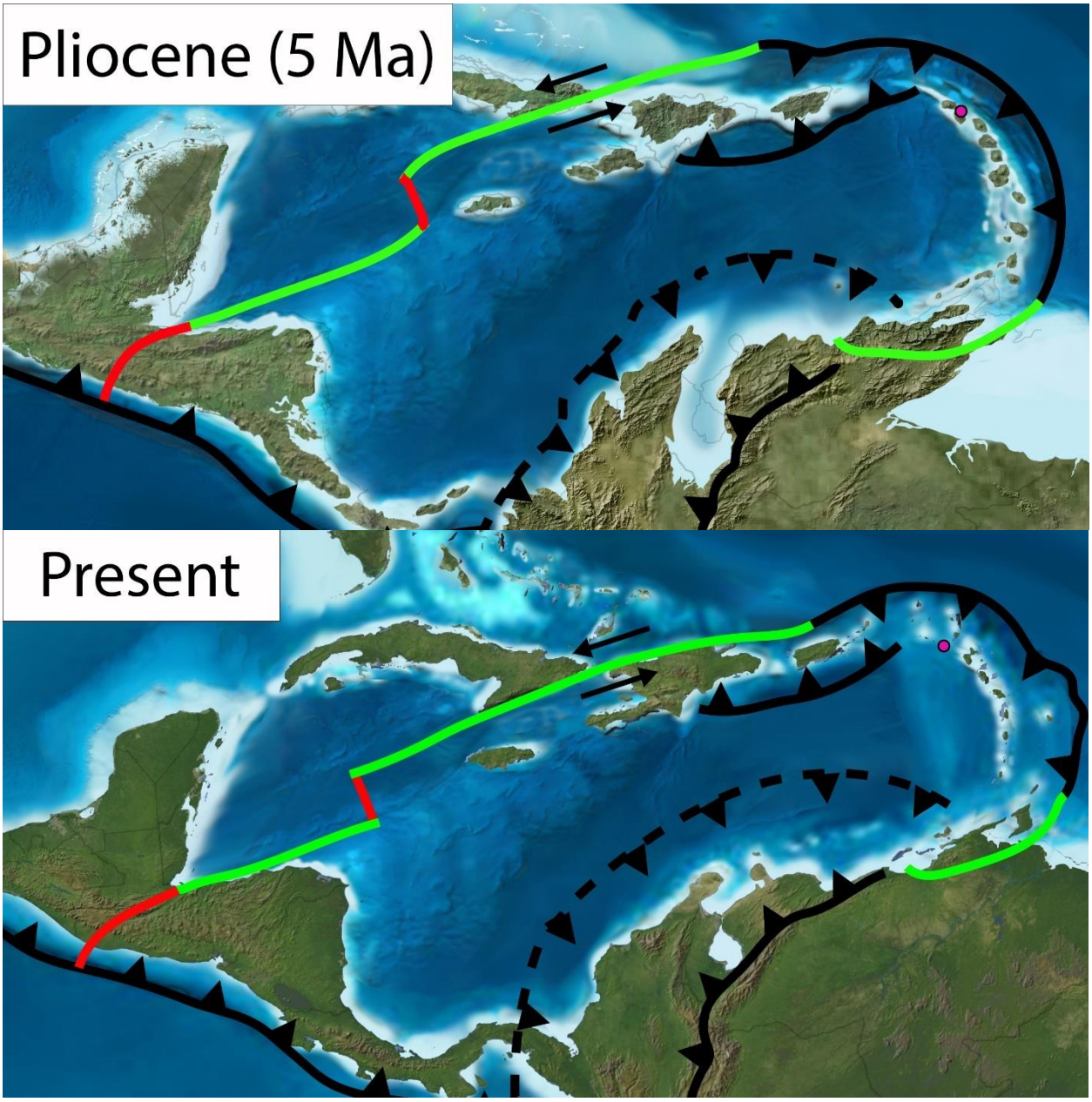

Figure 2. A tectonic evolution of the Lesser Antilles Arc and the surrounding region adopted from Blakey et al. (2009). Black lines with tooth marks indicate convergent boundaries. Green lines indicate transform boundaries, with black arrows designating the relative directions in which the plates move. Red lines indicate divergent boundaries. Boundary lines are dashed where inferred. Fuscia point indicates the location of Montserrat. Boundaries adopted from Garmon et. al. (2017).

Montserrat (16º45'N, 62º10'W) is part of the northern section of the Lesser Antilles Arc, the Leeward Islands (to the south are the Windward Island and Leeward Antilles Islands). The Leeward Islands contain two distinct volcanic island arcs of different ages. The outer arc is an older (40 mya) archipelago, easternmost of the two sections (Figure 1). The inner, younger arc (20 mya) is still active with repeated, explosive eruption of viscous, volatile-rich magma produced by the subduction processes, and contains the island Montserrat (Garmon et al., 2017). The SS-SH, Centre Hills, and Silver Hills volcanic complexes of Montserrat are three of 19 complexes still active in the Lesser Antilles Arc. Potential eruptions from these volcanoes present a risk to local populations, and accurate hazard assessments on the eruptive history of both large and small eruptions are necessary to be prepared for future eruptions. Therefore, providing a thorough geochemical analysis of volcanics from Montserrat is important in understanding Montserrat's volcanic and geologic history, and future. Variation in the composition of glass particles within a cryptotephra unit, specifically, can clue us into whether or not the magma chambers which feed SS-SH, Centre Hills, and Silver Hills are evolving, how they evolve over time scales of 1 to 10 million years, and how this evolution has an impact on the eruptive style (i.e. explosive vs. effusive).

Terrestrial volcanic deposits from SS-SH have a mineralogical assemblage comprising sodium-rich feldspars and some biotite, with basaltic lava flows comprised mainly of olivine, pyroxene, amphibole, and both sodium and calcium-rich feldspars (Devine et al., 1998; Rutherford & Devine, 2003). The island is littered with welded tuffs, pumice, tephra, and pyroclastic breccias, indicative of Vulcanian style eruptions (short and violent explosions of viscous magma) (Rutherford et al., 1998). Our current understanding of the SS-SH volcanic complex is owed to researchers including Malcolm J. Rutherford, John D. Devine, and Stephen

Sparks, whose work during and following the 1995-1998 eruption was integral to our current understanding of magmatic evolution during ascension, the formation and evolution of lava domes, and phase equilibria and reactions associated with explosive, andesitic eruptions. Their studies of the SS-SH volcanic complex are extensively referenced and used for comparison in this project and are crucial in allowing us to better grasp the implications of the geochemical results of this study. A summary of these results is provided below.

Increased seismic activity was recorded during the years of 1933-1937 and 1966-1967, suggesting that this activity may have indicated the movement of magma beneath the volcano (Sparks et al., 1998). More earthquakes were recorded from 1992 to 1994, but no seismic activity was actually observed leading up to the 1995 eruption (Sparks et al., 1998). The volcano initially erupted in the form of phreatic explosions and cold base surges. Tephra deposits generated by this initial eruption do not show any evidence of glass shards that indicate the presence of new magma, but SO_2 flux measurements said the opposite (Sparks et al., 1998).

Following the phreatic eruptions, in January 1996 the extrusion rate of the dome was significantly accelerated. Pyroclastic flows were consequently generated from dome collapse, and they became more frequent and more destructive as dome extrusion rate continued to accelerate through July 1996. This accelerated dome growth was determined to be the result of magma ascent, caused by the intrusion of a gas-rich magma into the magma chamber feeding the SS-SH volcanic complex (Sparks et al., 1998). Geochemical characteristics of tephra and pumice deposits generated by the pyroclastic density currents confirm this hypothesis, as they show a significant difference range in glass composition within a single layer. Higher levels of magma ascent/production, seismicity, SO_2 flux, and dome growth continued through 1998, destabilizing the complex's southwest crater and generating more pyroclastic flows. These later events are the

ones that forced the evacuation and abandonment of Plymouth. Vulcanian eruptions occurred in late 1997 and early 1998, but by this time the dome growth had slowed and there was less output of volcanic material into the atmosphere (Sparks et al., 1998).

The volcanic complex is known to have erupted two other times in recent geologic history (2460 BCE and 1550 BCE), but marine tephra and cryptotephra deposits indicate that SS-SH has a much lengthier and more complex volcanic history than previously assumed. In addition, the two less-studied volcanic complexes (Centre Hills and Silver Hills) may have an extensive and complicated volcanic history. However, eruptive material on land is less readily available, due to the burial of such volcanic material underneath new eruptive material or chemical weathering and harsh tropical environments.

In comparison to the SS-SH volcanic complex, relatively little is known about the volcanic history of Centre Hills and Silver Hills. Silver Hills volcanic complex is similar to the SS-SH volcanic complex in that it contains a significant proportion of massive intrusive glassy andesite. Over time, superficial volcanic tuffs have been stripped off the complex by prolonged erosion, and what is left represents the comparatively deep-seated center of a Miocene or Pliocene volcano. The rocks of the Silver Hills complex therefore probably correspond to an older volcanic basement complex. $^{40}Ar/^{39}Ar$ dating suggests that this volcanic center was last active around 2.17–1.03 Ma (Hatter et al., 2018).

Slightly more is known about the Centre Hills volcanic complex; in fact, it has been inferred from the geologic record that Centre Hills displays some of the most violent eruptive events of any of the volcanoes on Montserrat. The oldest dated unit from Centre Hills is andesitic lava from an old lava-dome complex at the southern edge of Centre Hills, dated at 0.95 Ma (Harford et al., 2002). This oldest deposit was then followed by at least eight large explosive

eruptions (and additional smaller, dome-forming eruptions like the cryptotephra deposits observed in this study) which occurred between 0.95 Ma – 0.6 Ma. These produced andesitic pumice and frequent effusive eruptions of compositionally similar andesitic lava (Cassidy et al., 2012; Harford et al., 2002). The collapse and erosion of the volcanic complex has generated extensive andesite lava breccias around its flanks.

Centre Hills was also active from around 0.6 Ma – 0.4 Ma (Coussens et al., 2017). This stage of volcanism involved more explosive eruptions (like the previous eruptive cycle), including the largest-volume explosive eruption deposit on Montserrat, the Woodlands Bay pumice (Coussens et al., 2017). This deposit is interspersed with deposits from effusive, smaller andesitic lava-dome forming eruptions, much like the ones we observe in this study. The youngest explosive eruption deposit, the Attic Pumice, is distinctive in that its dacitic composition is more evolved than any other deposit associated with all of Montserrat's volcanic complexes. Coussens et al. (2017) identified this as the compositionally distinctive, full maturation of the volcanic system towards more silicic compositions. That study concludes that the Attic Pumice represents final eruptive event for Centre Hills.

1.5 Proposed Research

Montserrat's South Soufriere-Soufriere Hills volcanic complex was reactivated in 1995, leading to regular pyroclastic flows and lahars. The complex continues to present a significant danger to local populations, and knowing its eruptive history is vital to preparation for future eruptions. Marine cores collected offshore in the Caribbean Sea can give insight into ~4.5 million years of the eruptive history of the volcanic center (Wall-Palmer et al., 2015), rather than the limited ~100,000-year history available onshore. Specifically, the two layers in this study were deposited approximately 400,000 years ago (+/- 10,000 years) (Fraass et al., 2016).

Montserrat (Figure 1) is also part of the Lesser Antilles Arc, an island arc located along a subduction zone where the oceanic crust of the South American plate is being subducted under the Caribbean plate.

A significant number of analyses have been performed on ash particles from recent eruptions of the South Soufriere-Soufriere Hills volcanic complex (since 1995) that appear in pumices and tephra on land. Very little geochemical analysis has been performed on tephra and cryptotephra deposits in the Caribbean Sea, or on volcanic material from Centre Hills and Silver Hills. The Integrated Ocean Drilling Program (IODP) expedition 340 successfully cored site U1396 (16830.49^{0}N, 62827.10^{0}W; 801 m water depth), a site which contains multiple tephra and cryptotephra layers. Deciphering the geochemistry of these deposits is necessary for understanding whether or not the tephra chemical composition is changing over time. It will also be useful to compare it to other geochemical analyses previously performed on tephra from Montserrat and other volcanoes in the Lesser Antilles Arc, providing a more in-depth knowledge of magmatic evolution in the arc.

I will evaluate the volcanic history of Montserrat and study the geochemical evolution of the magma storage region that feeds the Lesser Antilles Arc using two cryptotephra layers from core U1396C-1H-4W (11-15 cm and 41-45 cm downcore) with the following techniques:

1. Disaggregating and point counting samples in 0.5 cm segments to verify the presence of cryptotephra, by quantifying the proportion of glass particles, pumice, and juvenile volcanic material relative to other volcanic particles, similar to Fisher (2015).
2. Examining the variations in color, size, and texture of the glass and mineral particles associated with cryptotephra deposits.

3. Collecting major and minor element data using EPMA mainly for glass particles, but also on some mineral grains as well.
4. Collecting trace element data using SIMS for the same glass and mineral particles identified during EPMA.

2 | ANALYTICAL METHODS

2.1 Point Counting

In the background fraction of the core, volcanic clasts are dominated by glass and crystal fragments, so high percentage counts of volcanclastics apart from glasses will yield peaks when analyzed in the VSWIR (Visual Short Wave Infrared) spectral region (Fisher, 2015). Consequently, using glass particles and crystal fragments to identify a cryptotephra layer in one of these sediment cores could yield inaccurate interpretations, as these fragments can be found in any submarine sedimentary deposit (Cassidy et al., 2014). However, Cassidy et al. (2014) noted that non-vesicular lava clasts are at least somewhat reliable (five times out of nine) in correlating with peaks, an observation verified by Fisher (2015), who also added that the abundance of vesicular pumice often correlates with a cryptotephra layer. This section details the methods used for point counting particles to determine whether they correspond to a cryptotephra layer or not. I use an identical method to that of Fisher (2015), and a more in-depth description of the procedure can be found in that publication.

2.1.1 Sample Collection

After VSWIR analysis, each potential cryptotephra layer (and subjacent and superjacent strata) were sampled from the center of the working half of each core using two 2 x 2 x 2 cm samplers. Samples were collected such that two adjacent sample cubes, spanning 4.0 cm across the center of the core, collected approximately 1.0 cm^3 of sediment above and below the potential layer. For the core regions sandwiching the identified potential cryptotephra layer, approximately 2.0 cm^3 of sediment above and below were collected.

2.1.2 Sample Preparation

The methodology for sample preparation has been adapted from Blockey et al. (2005) to separate tephra particles and non-carbonate sediment from organic, pelagic sediment composed primarily of carbonates, such as microfossils and hemipelagic mud. Each 8.0 cm^3 cube was divided into 0.5 cm sections such that four 2.0 cm^3 downcore sample intervals passed through the identified cryptotephra layer (Figure 3B). This allows for fine (0.5 cm^3) resolution detection and characterization of any variations in tephra abundance with depth.

Before beginning the dissolution process, the mass of each 2.0 cm^3 segment was measured. Each 2.0 cm^3 segment was then placed into a 100 mL beaker on top of a hot plate at approximately 50^{o}C and was dissolved in 10% HCl for three days (Figure 3D, E). This is necessary as a majority of each interval comprises carbonate particles, which must be removed in order to allow for rapid identification of volcaniclastics. The samples were stirred about every 12 hours to enhance mixing and dissolution. Samples were then allowed to settle, decanted after centrifuging in test tubes, and rinsed in water several times to remove acid residues, allowing for more accurate geochemical analyses. The resulting non-carbonate material was wet sieved in a stainless-steel sieve to separate the >45 µm sediment fraction from the ultra-fine material (Figure 3F). Sediment fractions were then dried at room temperature (~25^{o}C) to prevent further alteration. The samples were then dry sieved using a brush and a USA Standard Test Sieve No. 325 (45 µm) to remove any remaining ultra-fine particles. The brush was used to stir the sediment and force all < 45 µm particles through the sieve.

2.1.3 Point Counting Procedure

The >45 µm sediment fraction was point counted using methodology and volcaniclastic classifications adapted from Le Friant et al. (2008), Cassidy et al. (2014), and McCanta et al. (2015), using a gridded black microfossil tray. For each 2.0 cm^3 of sediment, exactly 500

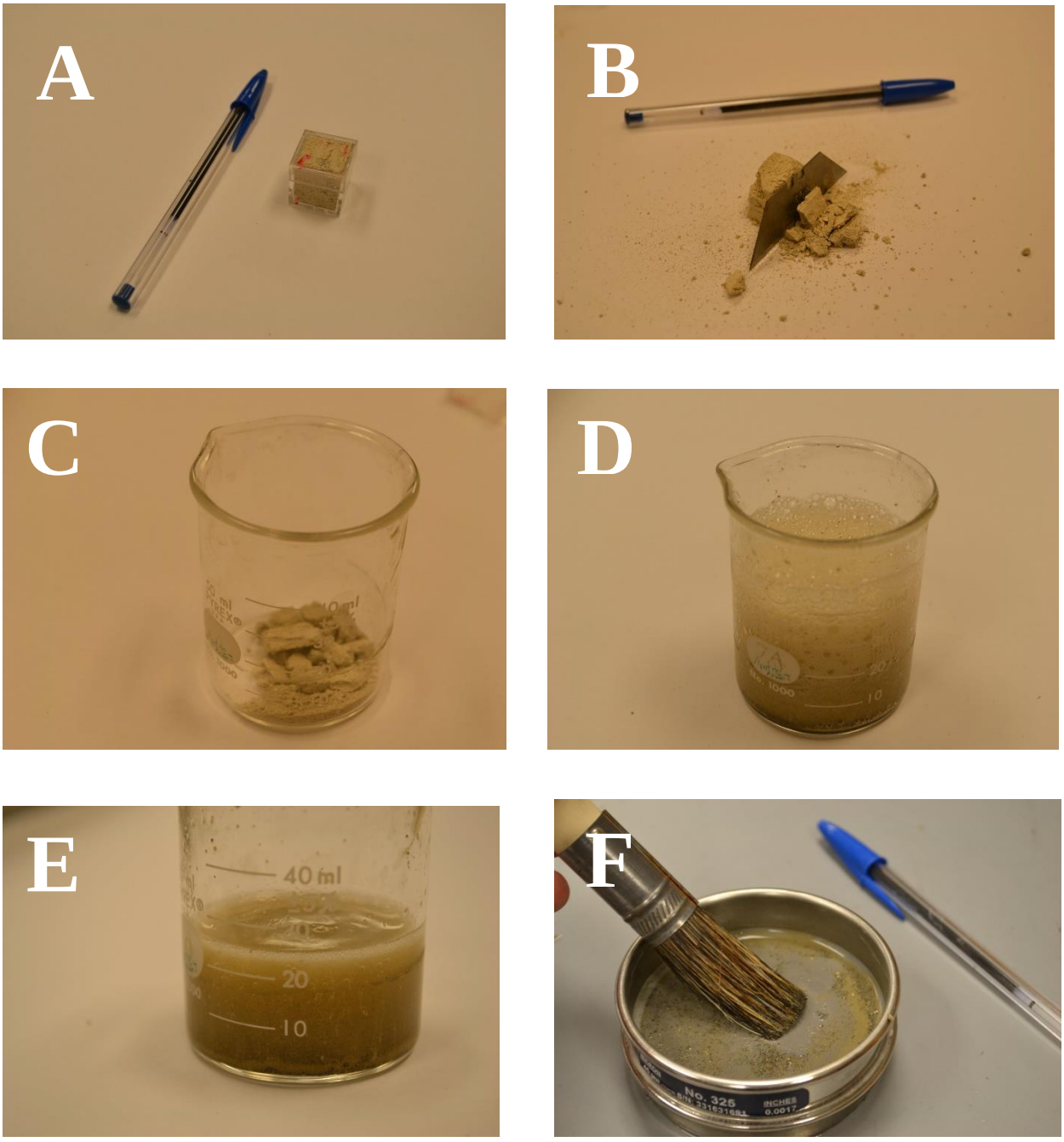

Figure 3. Documentation of the separation procedure. **A.** A photo of one 8.0 cm^3 cube prior to separation and dissolution, in its casing. Pen for scale. **B.** The crude method by which separation into 2.0 cm^3 blocks is performed, using an X-Acto ® blade. **C.** One 2.0 cm^3 block in a beaker just prior to dissolution. **D.** One 2.0 cm^3 block, five seconds after HCl is added to the beaker. **E.** One 2.0 cm^3 block, fifteen minutes after the addition of HCl. **F.** Wet sieving the remaining portion of the dissolved and cleaned 2.0 cm^3 block, using a sieve brush.

particles were counted and classified as either (1) white glass/mineral fragment, (2) dark glass/mineral fragment, (3) vesicular pumice, (4) non-vesicular lava clast, (5) altered lava clast, or (6) scoria. Bioclasts, silica tests of diatoms and radiolarians, and other suspected biogenic particles were not counted. The six main classifications were selected so particles could be identified with a strong degree of confidence, as variance of particle types represent different eruptive conditions (or lack of eruption) and can be used to interpret the type of volcanic eruption that produced them. In addition, these methods allow for results to be directly compared with results from related cryptotephra studies (Cassidy et al., 2014).

Volcanic glass shards and white mineral fragments were classified on transparency and color (Figure 4A). If the particles were white, grayish-white, clear, or stained slightly yellow or green, they were classified as white glass/mineral. A petrographic microscope can be used to further divide this category into two subcategories of white glass and white mineral, but for the purpose of this study the two were not distinguished. Black glass/minerals were classified primarily on color and crystallographic nature (Figure 4B, C). Black minerals especially are easily identifiable due to well-defined cleavage planes characteristic of pyroxene and amphibole. Vesicular pumice can be differentiated from white glass due to its morphology/texture, lack of transparency, composition, and petrographic characteristic (lack of crystallinity) (Figure 4D). Pumiceous material tends to be highly vesiculated and opaque, sometimes with multiple colors and compositions, in which color tends to be a function of composition. Non-vesicular lava clasts vary in size and shape, and color and opacity were mainly used to identify them. Lithic fragments in this category should be unaltered (there is a separate “altered” classification), and in general contain a fine-grained white and translucent matrix with interspersed dark crystals (dark green, red, brown, and black). Morphologically, altered lava clasts are almost identical to non-

vesicular lava clasts, except they are altered (i.e. they exhibit a change in color) (Figure 4E). Lithic particles that are altered are entirely red (indicating oxidation), as opposed to only having a few grains that are red or dark in color. Highly vesiculated, dark (grey to light grey) particles were classified as scoria (Figure 4F). Textural features are similar to that of vesicular pumice, with either spherical or angular vesicles and a felty surface.

After point counting the particles, counts were compared to the mass of the pre-dissolved material as follows:

$$\frac{number\ of\ counts\ (white\ glass, black\ glass, etc.)}{mass\ of\ predissolved\ sediment\ (g)} = \frac{counts}{gram}$$

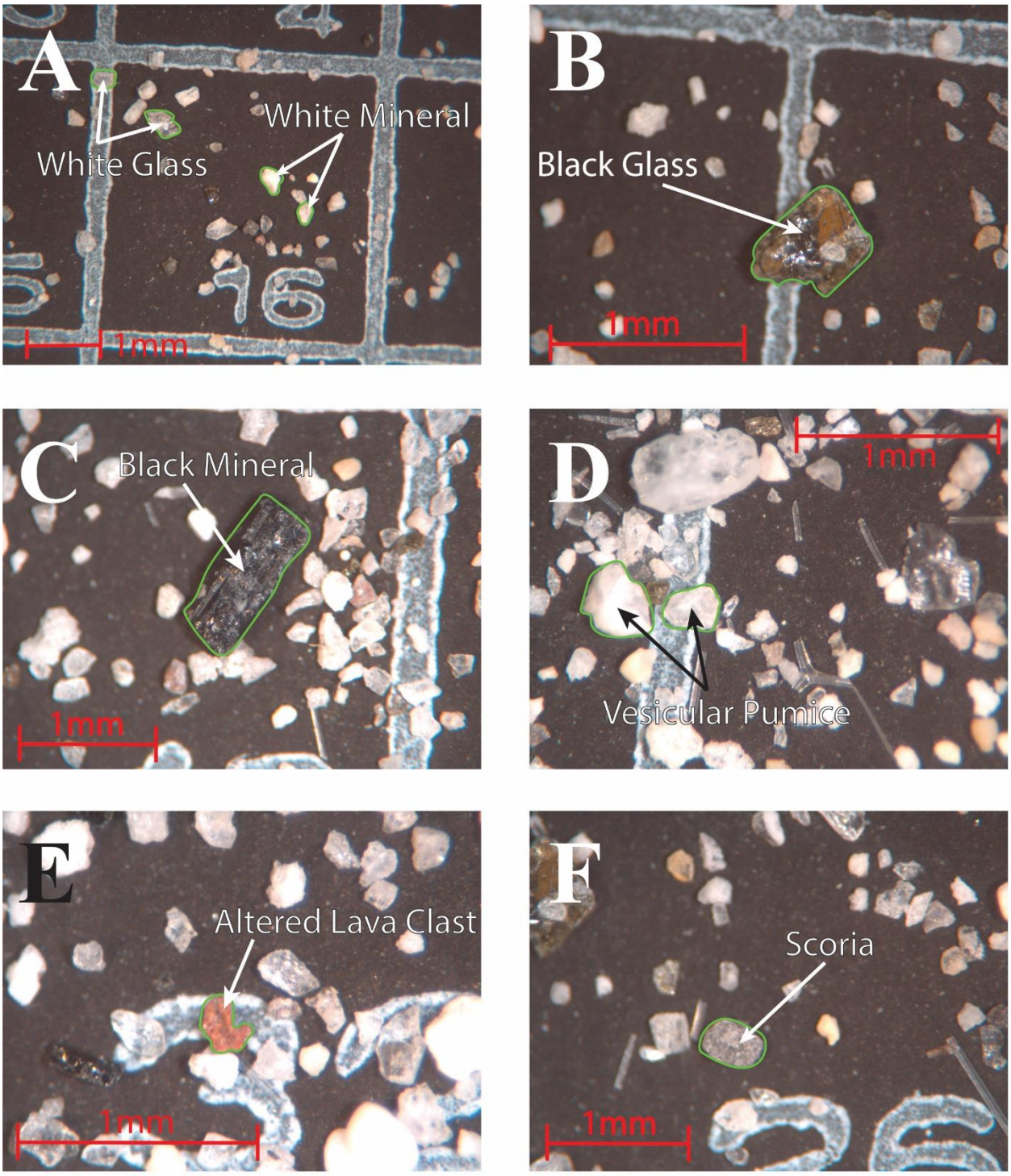

Figure 4. Binocular photos of cryptotephra particles **A.** white glass and white mineral fragments are circled in green. **B.** a black glass fragment is circled in green. **C.** a typical black mineral (in this case, amphibole) is circled in green. **D.** vesicular pumice fragments are circled in green. **E.** a tiny, but representative altered lava clast is circled in green. **F.** a scoria particle, rare in these samples, is circled in green.

2.2 Scanning Electron Microscopy (SEM)

After point counting the grains and classifying them, they were examined using a JEOL 6300 scanning electron microscope. Micro-analyses helped confirm whether the samples were polished well enough for electron microprobe analysis, better assess the texture of the particles, determine which grains represent glass particles so they can be marked for electron probing and SIMS work, and qualitatively assess grain compositions.

2.2.1 Sample Preparation

Samples were prepared for SEM analysis using 1-inch round epoxy mounts. Using the lower portion of the mounting plug, I applied a piece of double sided tape and poured a thin layer of cryptotephra on top of the tape. A clean eraser was then used to imbed the layer of cryptotephra into the tape. This prevents low density particles from becoming buoyant while the epoxy is setting. I used Hillquist® Thin Section Epoxy, which cured at ~80^{o}C on a hot plate for two hours. I then polished off the tape using a Buehler MiniMet polishing machine. Samples were then carbon coated.

2.2.2 Analytical Procedure

Samples were analyzed using the SEM at the Tufts University Department of Earth and Ocean Sciences and the Revolution software package for data reduction. Back scatter electron (BSE) images, secondary electron images (SEI), and initial quantitative chemical analyses for Si, Ti, Al, Mg, Fe, Au, Ca, Na, and K were acquired using Energy Dispersive Spectroscopy (EDS) to generate X-ray intensity maps for the grains. Material analyses were obtained using a 15 kV acceleration voltage, 10 nA beam current, and a defocused beam (diameter = 5-15 µm). I did not calibrate the machine for these analyses, and the chemical results are not reported as their purpose was primarily to assess which grains to target for microprobe analyses.

2.3 Electron Probe Microanalysis (EPMA)

2.3.1 Analytical Procedure & Data Reduction

The electron microprobe method was used to investigate the major and minor element glass and mineral geochemistry. Samples were irradiated with a beam of electrons, consequently exciting electrons on the surface of glass and mineral particles. The movement of electrons on the surface emits photons of energy that are detected by spectrometers; each element releases a unique photon, and therefore we can use EPMA to identify major and minor elements present in a glass particle, and their concentrations.

Analysis by electron microprobe was conducted using the JEOL-JXA-8200 Superprobe at the Department of Earth, Atmospheric, and Planetary Sciences at the Massachusetts Institute of Technology. I determined the major and minor element composition (S, Al, P, Mn, Na, Ti, Si, K, Fe, Mg, Cr, Ca, Ni) in oxide weight percent of the glasses and minerals in the cryptotephra layers. I used an accelerating voltage of 15 kV, a beam current of 10 nA, and a spot size of 10 µm. The count time was 10 seconds for Na, and 40 seconds for all other elements. The matrix correction program CITZAF (a program for the quantitative electron microbeam X-ray analysis of thick polished materials, thin films, and particles) was used for our analyses (Armstrong, 1995). Standardization conditions were checked using MORB glass Alvin 1690-20. MIT's analytical facilities do not have a high-silica glass standard, so a MORB glass with the highest possible silica concentration available was used instead.

The low count time for Na is due to the need to minimize the potential for remobilization and loss of Na (a volatile element). High SiO_2 glass particles are expected to contain 3-10 wt. % water, which cannot be detected via EPMA. Therefore, any analytical points yielding totals greater than 90% were accepted. I were able to discriminate glass particles from mineral

fragments based on total oxide weight percent, and also the abundance of major elements like Al, Ca, Fe, and Mg. For example, if we had 10.5% MgO, that point was most likely taken on a pyroxene grain.

For the purpose of this study, we analyzed more glass particles than minerals. Glass refers to samples where analyses have been taken on a clean, amorphous quenched melt with no visible phenocryst or melt inclusion phase. Such data provide information regarding the final geochemical state of the liquid magma body.

2.4 Secondary Ion Mass Spectrometry (SIMS)

2.4.1 Analytical Procedure

SIMS is an analytical technique which uses a phenomenon called sputtering. Energetic ions impinge upon a solid that inevitably leads to the ejection of particles off the surface of the glass or mineral (Zalm, 1994). These liberated species carry information about the surficial composition of the glass/mineral, and therefore the sputtered secondary species then reflects the composition of the glass/mineral surface (Zalm, 1994). Given a sufficient mass resolution, a perfect mass separation allows for the detection of any element and its isotope(s), which is unique for surface sensitive analytical techniques.

Rare earth element, and other trace element data were collected using the Cameca IMS 3f at the Woods Hole Oceanographic Institution for glass particles. The following isotopes were analyzed: ^{26}Mg, ^{30}Si, ^{39}K, ^{49}Ti, ^{85}Rb, ^{88}Sr, ^{89}Y, ^{138}Ba, ^{139}La, ^{140}Ce, ^{141}Pr, ^{143}Nd, ^{147}Sm, ^{151}Eu, ^{157}Gd, ^{159}Tb, ^{163}Dy, ^{165}Ho, ^{167}Er, ^{169}Tm, ^{171}Yb, ^{174}Yb, and ^{175}Lu. Counts were normalized to pre-determined ^{30}Si concentrations collected via EPMA and used to calculate absolute elemental concentrations in the glass particles. Systematic drift was monitored by sequential analyses of solid reference materials from the MPI-DING series: ATHO-G, T1-G, and StHs-6/80G.

4 | RESULTS

4.1 Relative Abundance of Certain Particles

Point counting results for the 11-15 cm and 41-45 cm segments of core U1396-1H-4W are reported in Appendix A. Results are first displayed as the amount of each particle type counted out of 500 total particle counts. Then, each particle type is represented as the total amount of counts per gram of undissolved sediment. A brief description of the point counting results is provided below.

In the 11-15 cm segment, white glass/mineral and vesicular pumice were the two most common particles types observed, and each segment interval contained similar amounts of vesicular pumice and white glass/minerals (~ 40 – 45 % for white glass/mineral, ~ 40 – 45 % for pumice). The next most abundant particles are dark glasses and non-vesicular lava clasts (~ 4 – 7 % for both). Altered lava clasts and scoria occur in relatively minor amounts (~ 1 – 3 %).

In the 41-45 cm segment, white glass/mineral was the most common particle type observed (always > 50 %). There were relatively low amounts of vesicular pumice observed in this segment of the core than there was in segment 11-15 cm (~ 20 – 30 %). The next most abundant particle type was vesicular pumice, followed by dark glass (~ 10 %, 8 % respectively). Dark glass is found in similar yet slightly higher amounts than it is in the 11-15 cm core segment. Non-vesicular lava clasts, altered lava clasts, and scoria were also observed in similar amounts as they were in the 11-15 cm core segment.

4.2 Glass Color & Texture

For the *white glass/mineral* category, particle size and rounding varied widely, although glassy particles do tend to be more angular (Figure 4). Primary morphologies included clear, angular shard particles; clear, moderately vesiculated particles; translucent, white-to-gray,

vesiculated particles that are indistinguishable between glass or mineral; plagioclase grains (Figure 5C, D, E); and transparent green-to-yellow elongate particles with a moderately columnar shape. Particles that contained inclusions of oxides or red oxide staining were included in this classification, as the dominant crystal phase was either white glass or white mineral. Most of the particles included in this classification are slightly colored and transparent; they tend to be glass particles, and they have an amorphous nature and lack cleavage and structure.

Like with the white glasses/minerals, *dark glass/mineral* particle size varies, but the shape is generally angular due to well-defined cleavage planes in members of the pyroxene and amphibole groups. Conchoidal fracture is common along crystal boundaries for obsidian particles (Figure 4). Color in this classification group ranges from dark green to dark brown or black, and particles tend to be either translucent or opaque. Minerals that have fractured along a cleavage plane tend to show a vitreous luster, but this is not always the case as weathering can dull the surface. Grains tend to be euhedral, but several are subhedral in nature as well, displaying damaged and irregular textures. However, while the display of a crystal face may be a good way to identify these mineral fragments, color is still the best way to identify these particles, as their optical properties and anisotropy in polarized light differ sharply from any of the other particle classifications explored in this study. I also classified mineral grains that were bright red and euhedral as black glass/mineral. The bright red color is likely due to the extreme oxidation of mafic minerals. Black glasses/minerals are common in these samples, as the composition of tephra tends to be andesitic in nature.

For *vesicular pumice* particles, our samples range in color from white to gray, beige, yellow, tan, and pink-to-red if oxides are present (Figure 4). Particles of this group tend to have a highly irregular surface texture and lots of open pore space. These highly vesiculated, glassy

particles don't transmit light and don't display clear grain boundaries. They exhibit a "fluffy" texture that is distinct from lithic clasts, mineral grains, and glass particles (Figure 4A, B). Particles can also exhibit a multicolored appearance, suggesting that they contain multiple different microcrystals or have been altered via staining. They also have a fibrous appearance to them. In rare cases, particles are beige-to-light yellow, and appear at first glance to be lithic particles. Upon comparison to a highly vesiculated, glassy pumice grain, they display similar characteristics under a petrographic microscope (i.e. they do not transmit light readily). Luster is not a reliable method to classify vesicular pumice, as it can range from dull to bright and vitreous. Fisher (2015) noted that the luster is dependent on the vesicularity of the particles in her study, however, I did not see a similar correlation in these samples. That previous study also noted a strong degree of ambiguity in identifying pumice, a similar problem encountered in this study; SEM analysis resolves this issue (Figure 5).

For *non-vesicular lava clasts,* crystals are present in almost all lithic fragments. However, there are a few cases in which fragments contain only a white, translucent matrix. I also found very few examples of coarse-grained white, translucent material, which was classified under non-vesicular lava clast. I also found several fine-grained particles resembling basalt, and they were placed into this category. In this group, luster varies from glassy to waxy, and shape varies from sub-rounded to sub-angular. Non-vesicular lava clasts, and consequently altered lava clasts, are differentiated from pumice based on particle shape and morphology; lava clasts tend to be less angular, and less vesiculated. However, analysis via SEM determined that some lava clasts are fairly vesicular (Figure 5F).

Most *altered lava clasts* observed in these samples were red in color (Figure 4). Lithic particles that have been altered to other colors (yellow, green-ish, tan) are also included in this

category. Particles tend to contain black or tan crystals as inclusions or lithic fragments. Particles are translucent, just like unaltered clasts, but tend to be slightly more opaque.

Scoria is not particularly common in these samples as it tends to be derived from mafic material, and the magma from which these tephra samples are derived is primarily andesitic in composition. Some scoria particles contain inclusions of lithic fragments. I also included scoria particles that were altered due to oxidation.

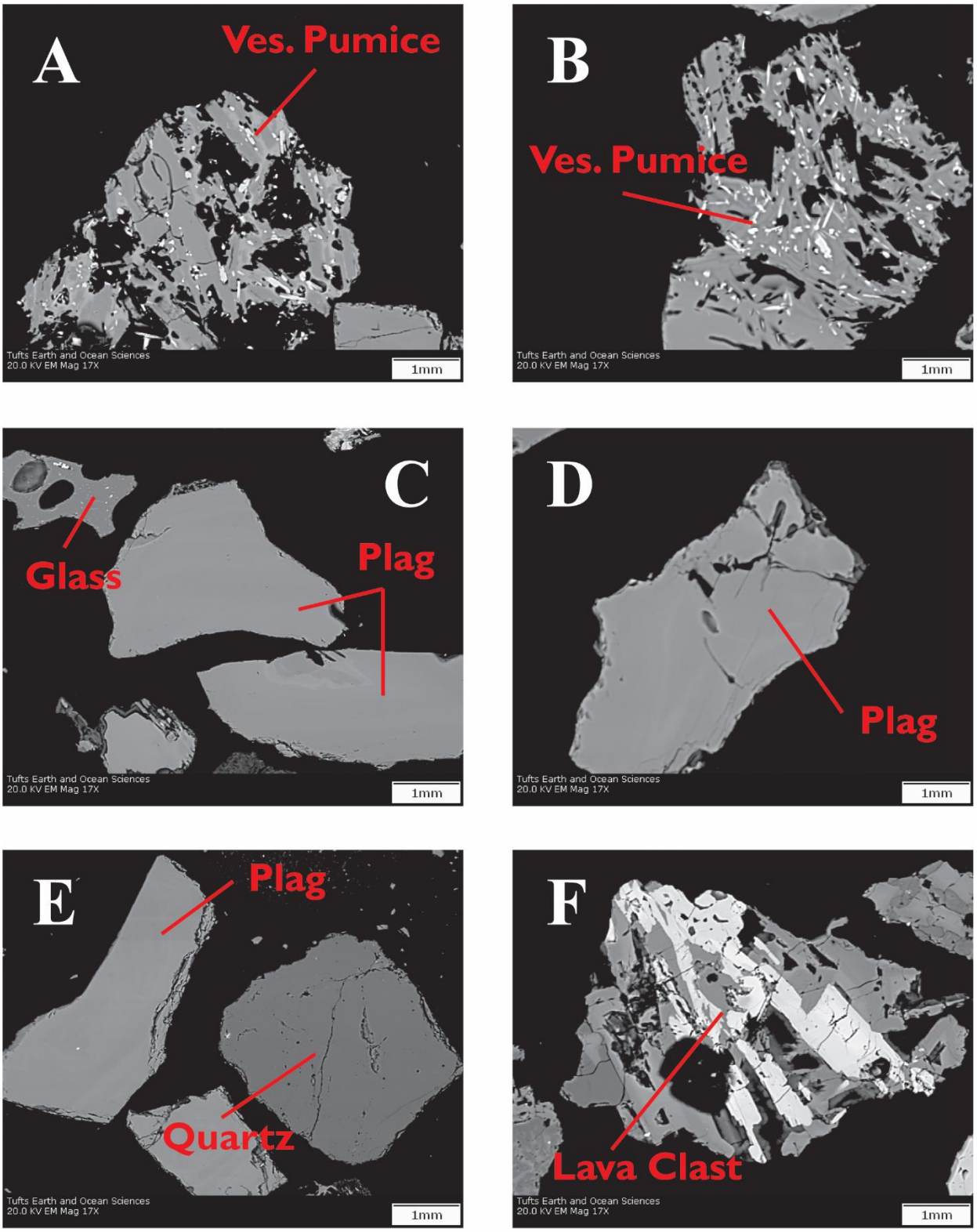

Figure 5. BSE images obtained via SEM which detail the textural and mineralogical characteristics of cryptotephra particles from core U1396-4H-4W. **A.** Disaggregated vesicular pumice particle. **B.** Disaggregated vesicular pumice particle. **C.** Glass particle and plagioclase grains. **D.** Plagioclase grain. **E.** Plagioclase and quartz grains. **F.** Non-vesicular lava clast.

4.3 Glass Chemistry

The results of major, minor, and trace element chemistry for individual glass particles of the 11-15 cm and 41-45 cm sections of core U1396C-1H-4W are tabulated in Appendices B and C. The chemical characteristics of glass particles for each core interval are described below. Data plots for both the 11-15 cm and 41-45 cm core segments are presented in Figures 6A-E, showing SiO_2 (wt. %) vs. NaO + K_2O (wt. %), CaO (wt. %), Al_2O_3 (wt. %), TiO_2 (wt. %) and Mg# (Mg/(Mg+Fe)).

4.3.1 Interval 11-11.5 cm

The composition of glass particles in this core interval varies significantly depending on which particle the analysis was taken on. SiO_2 content varies from 66.21 to 77.65 wt. %, TiO_2 content varies from 0.0649 to 0.884 wt. %; these values tend to increase with decreasing SiO_2 content. MgO and FeO content varies from 0.04 to 1.06 and 0.65 to 4.20, respectively; again, these values tend to increase with decreasing SiO_2 content. Mg# values range 4.84 to 37.10, which is expected for particles derived from a chemically evolved source. Na_2O and K_2O content varies from 0.44 to 4.30 and 0.13 to 2.87, respectively; total alkali content values tend to increase with increasing SiO_2 content, a trend that is consistent with TAS (Total Alkalis vs. Silica) diagrams. Apart from SiO_2, Al_2O_3 content is the most abundant in these glass particles (and for all other intervals too). Like the other major and minor elements present, its content decreases with increasing SiO_2 content. Total contents range from 92.22 to 98.45 wt. %. It is assumed that OH, H_2O, and CO_2 comprise the remaining amount of these glass particles. Trace element chemistry was not collected for this core interval. Cr_2O_3, SO_3, and NiO are below detection limits.

4.3.2 Interval 11.5-12 cm

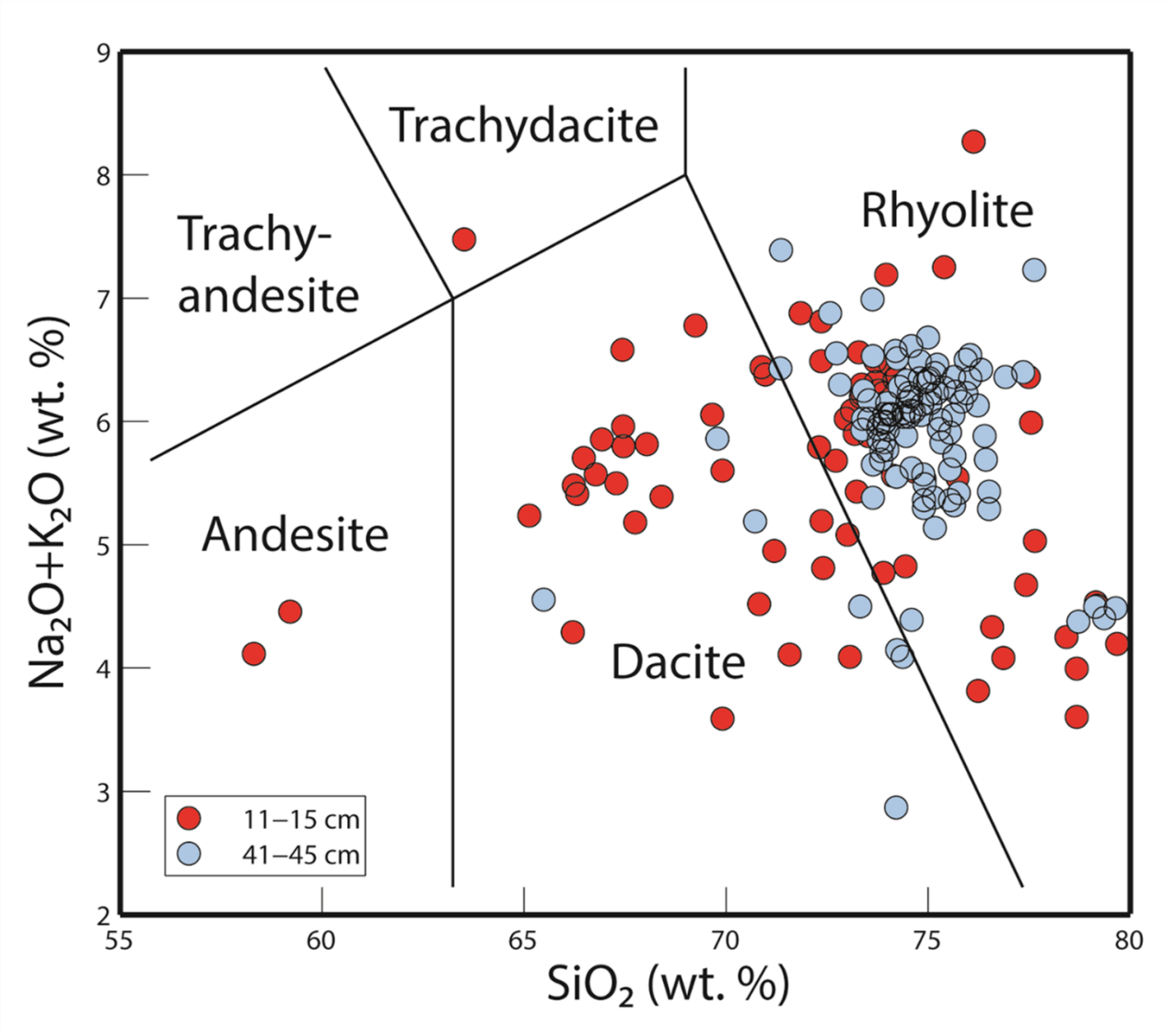

Figure 6A. TAS (Total Alkali Silica) Diagram showing the values of SiO_2 (wt. %) vs. NaO + K_2O (wt. %) for the 11-15 cm and 41-45 cm core segments. The average trend is an increase in total alkali content as silica increases.

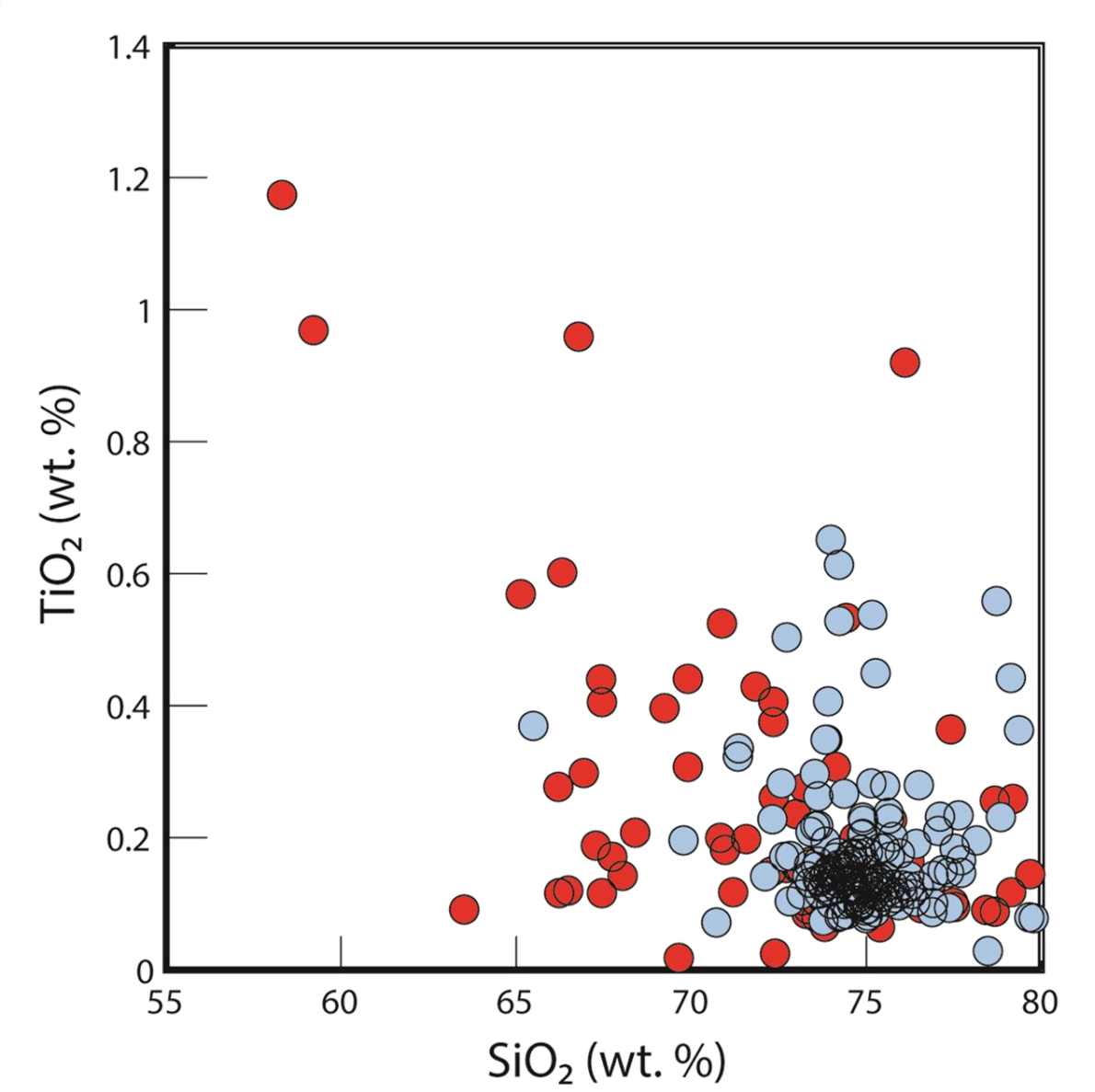

Figure 6B. Harker Diagram showing the values of SiO_2 (wt. %) vs. TiO_2 (wt. %) for the 11-15 cm and 41-45 cm core segments. The average trend is an decrease in TiO_2 content as silica content increases.

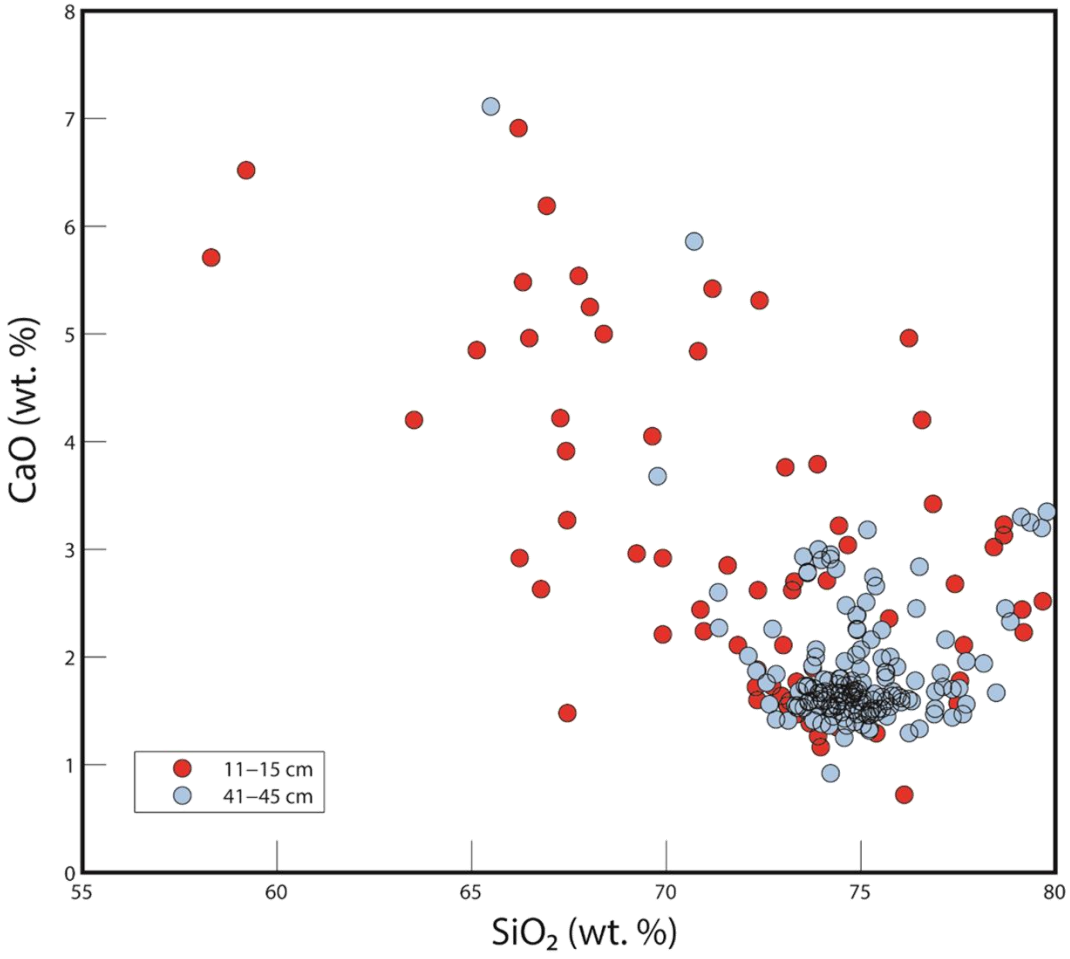

Figure 6C. Harker Diagram showing the values of SiO_2 (wt. %) vs. CaO (wt. %) for the 11-15 cm and 41-45 cm core segments. The average trend is a decrease in CaO content as silica content increases.

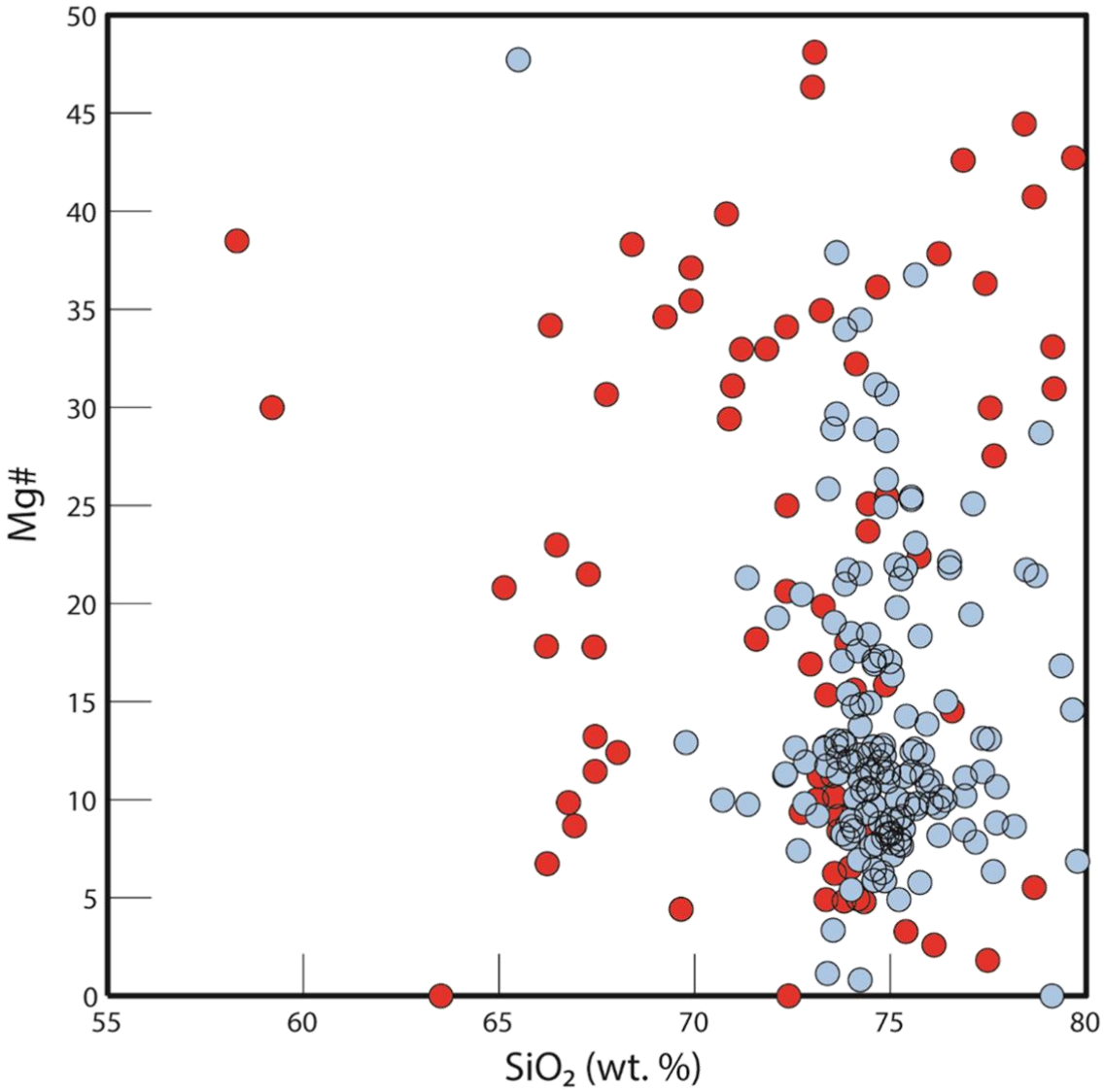

Figure 6D. XY plot displaying the values of SiO_2 (wt. %) vs. Mg# for the 11-15 cm and 41-45 cm core segments. There is a slight average trend towards a decrease in Mg# as SiO_2 content increases. Higher Mg# values indicate more geochemically 'primitive' quenched melts.

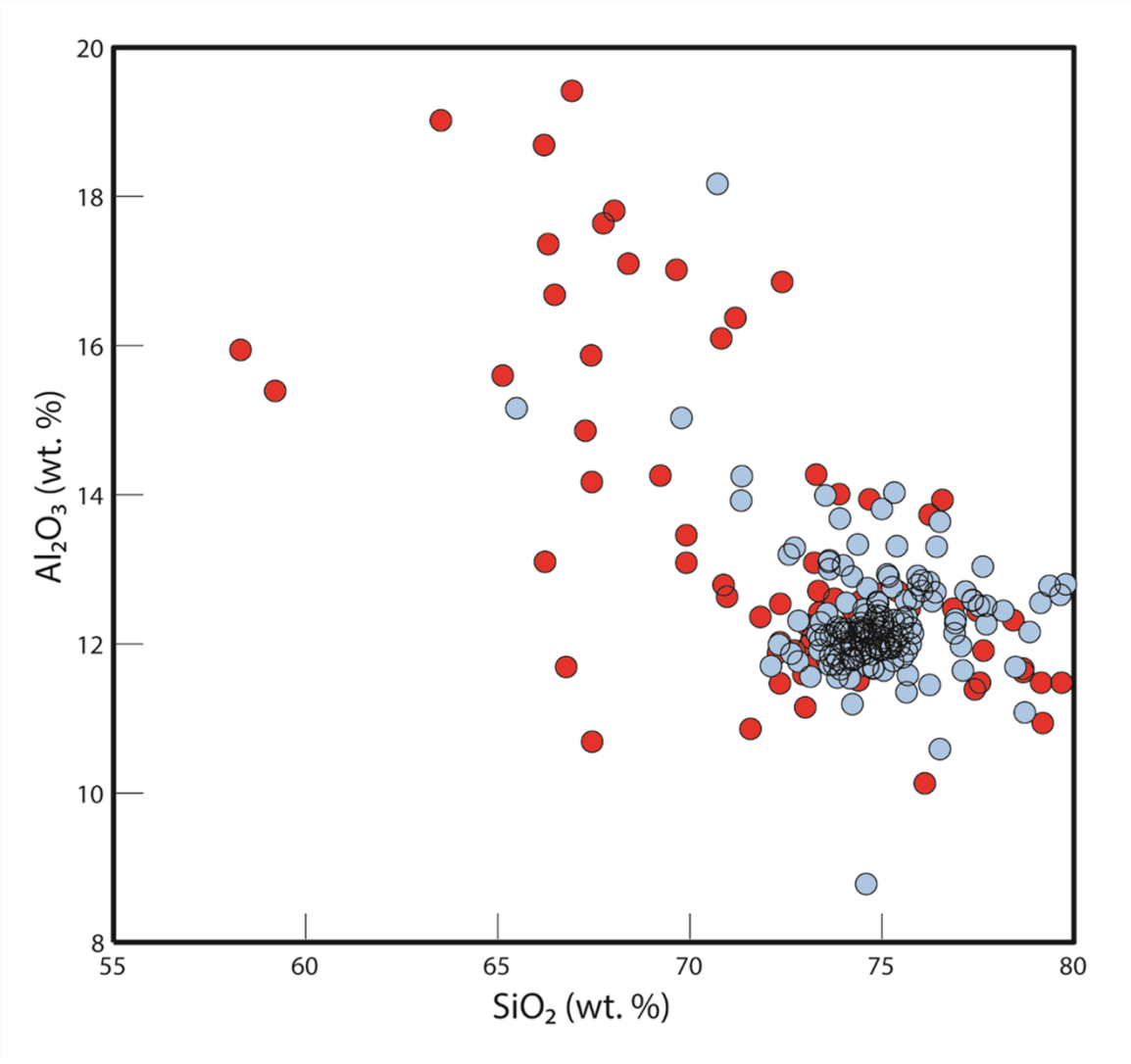

Figure 6E. Harker Diagram showing the values of SiO_2 (wt. %) vs. Al_2O_3 (wt. %) for the 11-15 cm and 41-45 cm core segments. The average trend is a decrease in Al_2O_3 content as silica content increases.

As with the last interval, the composition of these glass particles varies significantly depending on which particle the analysis was taken on. SiO_2 content varies from 67.28 to 78.68 wt. %. TiO_2 content varies from 0.11 to 0.96 wt. %, and these values tend to decrease with increasing SiO_2 content. This trend is also observed in FeO and MgO values, which vary from 0.62 to 7.64 wt. % and 0.08 to 0.53 wt. % respectively. Mg# values are relatively low again, ranging from 9.85 to 40.73 It is also observed in Al_2O_3 content; Al_2O_3 content varies from 10.86 to 17.10 wt. %. Na_2O and K_2O content varies from 3.39 to 4.49 wt. % and 0.21 to 1.85 wt. %, respectively; total alkali content values tend to increase with increasing SiO_2 content. Total oxide contents range from 90.40 to 97.68 wt. %. Again, we assume OH, H_2O, and CO_2 are the remaining chemical constituents of these particles, even though they cannot be detected via EMPA. Cr_2O_3, SO_3, and NiO were below detection limits. Trace element chemistry was not obtained for this interval of core U1396C-1H-4W.

4.3.3 Interval 12-12.5 cm

Similar to the other intervals, glass particle compositions vary significantly, particularly in their content of SiO_2 (wt. %). SiO_2 content varies from 65.13 to 79.68 wt. %. TiO_2 content varies from 0.12 to 0.92 wt. %, and these values tend to decrease with increasing SiO_2 content. This trend is also observed in FeO and MgO values, which vary from 0.72 to 4.66 wt. % and 0.03 to 1.25 wt. % respectively. Mg# values are relatively low again, ranging from 2.59 to 46.32. It is also observed in Al_2O_3 content; Al_2O_3 content varies from 10.86 to 17.10 wt. %. Total contents range from 95.64 to 99.08 wt. %. Na_2O and K_2O content varies from 3.03 to 4.96 wt. % and 0.32 to 5.24 wt. %, respectively; total alkali content values display the typical trend of increasing with increasing SiO_2 content. This interval does not vary too much in total content.

Again, the remaining chemical constituents are assumed to be OH, H_2O, and CO_2. Cr_2O_3, SO_3, and NiO are below detection limits. Trace element chemistry was not obtained for this interval.

4.3.4 Interval 12.5-13 cm

Glass particle composition in this interval varies even more significantly than other intervals. SiO_2 content varies from 66.23 to 90.28 wt. %. TiO_2 content varies from 0.02 to 0.30 wt. %; this is a relatively small variance in comparison to the other elements analysed via EPMA, and the usual trend of TiO_2 content decreasing with increasing SiO_2 content is not as pronounced in this interval. FeO and MgO content varies from 0.25 to 1.98 wt. % and 0.02 to 1.19 wt. % (some values were below the detection limit and are reported as 0). Mg# varies from 6.74 to 57.95. The latter is a relatively high Mg# for the particles we are analyzing. Na_2O and K_2O contents vary from 1.27 to 5.12 wt. % and 0.23 to 2.23 wt. %, respectively. Total alkali content values increase with increasing SiO_2 content. Cr_2O_3, SO_3, and NiO are present in very minor amounts. Total content varies from 89.85 to 100.57 wt. %, the highest variance reported yet. It is not expected for glasses to yield 100% total content, but overall composition of that one particle is typical of a high-silica glass, so it was kept in the dataset. Trace element chemistry was not obtained for this interval.

4.3.5 Interval 13.5-14 cm

More variance in glass composition is observed in this interval. SiO_2 content varies from values of 63.52 to 87.30 wt. %. TiO_2 content is not as significantly variant, with values ranging from 0.06 to 0.44 wt. %; there is evidence here for a trend in TiO_2 content decreasing with increasing SiO_2 content, but it is not as significantly pronounced as observed in other samples, described above. FeO and MgO contents vary from 0.43 to 2.83 wt. % and below detection limit to 1.47 wt. %, respectively. Mg# values range from below detection limit to 48.10. These

numbers are consistent with the chemically evolved nature of these samples. Na_2O and K_2O contents range from 2.28 to 6.33 wt. % and 0.25 to 4.53 wt. %, respectively. Total alkali content increases sharply with decreasing SiO_2 content, contrary to the results from other intervals. Al_2O_3 contents range from 7.41 (relatively low) to 19.02 wt. %. Cr_2O_3, SO_3, and NiO are present in very minor amounts. Total content varies from 94.59 to 99.31 wt. %, which is relatively low considering 25 different glass particles were analyzed, the largest for any interval of the 11-15 cm segment. Trace element chemistry was obtained using SIMS for this interval. Grains display both positive and negative europium anomalies and are relatively enriched in the light rare earth elements (LREEs) in relation to the heavy rare earth elements (HREEs) (Figure 7A).

4.3.6 Interval 14-14.5 cm

This interval contained only four glass particles that were successfully analyzed. Thus, we do not see a significant variance in the results. SiO_2 contents vary from 69.65 to 74.08 wt. %. TiO_2 contents vary from 0.02 to 0.43 wt. %, and this is the only interval of the 11-15 cm segment where TiO_2 content increases with increasing SiO_2 content. FeO and MgO contents vary from 0.37 to 2.86 wt. % and 0.01 to 0.79 wt. %, respectively. Mg# values range from 4.41 to 34.09. Na_2O and K_2O contents range from 3.21 to 5.73 wt. % and 0.31 to 3.60, respectively. Total alkali contents show no increasing nor decreasing trend when plotted against SiO_2 (wt. %). Al_2O_3 content ranges from 11.47 to 17.02 wt. %, values which decrease with increasing SiO_2 content. Cr2O3, SO_3, and NiO are below detection limit. Total content ranges from 96.20 to 97.47 wt. %, the lowest variance observed in any of the intervals in the 11-15 cm segment. Trace element chemistry was not obtained for this interval.

4.3.7 Interval 14.5-15 cm

The composition of glass particles varies significantly in this interval. SiO_2 contents range from 58.31 (the lowest values observed thus far) to 75.73 wt. %. TiO_2 contents vary from 0.08 to 1.17, and decrease with increasing SiO_2 content. FeO and MgO contents vary from 1.30 to 9.36 wt. % and 0.08 to 2.29 wt. %, respectively. These values tend to decrease with increasing SiO_2 content. Mg# values range from 4.80 to 39.86. Na_2O and K_2O values range from 3.76 to 4.84 wt. % and 0.28 to 2.58 wt. %, respectively. Total alkali content here tends to increase with increasing SiO_2 content. Al_2O_3 content varies from 11.39 to 16.68 wt. % and decreases with increasing SiO_2 content. NiO, Cr_2O_3, and SO_3 are present in very minor amounts. Total content ranges from 94.41 to 100.21 wt. %. Trace element chemistry was obtained using SIMS for this interval. Grains display both positive and negative europium anomalies and are relatively enriched in LREEs in relation to HREEs. One grain also displays a positive samarium anomaly (Figure 7B).

4.3.8 Interval 41-41.5 cm

The chemical composition of glass particles from this interval does vary, but not that significantly. SiO_2 contents range from 74.20 to 82.80 wt. %. TiO_2 content ranges from 0.03 to 0.20 wt. %. These are much lower contents than observed in the 11-15 cm section of the core, and they do not show any significant trend when plotted against SiO_2. FeO and MgO contents range from 0.26 to 2.14 and 0.03 to 0.28 wt. %, respectively. MgO contents particularly are lower than those observed in the 11-15 cm section of the core. Mg# values range from 4.80 to 39.86, which is expected for particles that originate from an evolved source. The Na_2O and K_2O contents range from 0.69 to 4.43 wt. % and 0.14 to 4.01 wt. %, respectively. Total alkali content increases with increasing SiO_2 content, a trend observed in some interval of the 11-15 cm segment of the core. Al_2O_3 content ranges from 10.08 to 12.59 wt. %; this is a smaller variance

observed than the 11-15 cm segment displayed. As is expected, these values decrease with increasing SiO_2 content. Trace amounts of Cr_2O_3, SO_3, and NiO are observed in these particles. Total content ranges from 95.02 to 100.87 wt. %. Trace element data was not obtained for this interval.

4.3.9 Interval 41.5-42 cm

Only a slight variation in the chemical composition is observed for this interval of the core in compared to the 11-15 cm segment. SiO_2 contents range from 72.11 to 78.85 wt. %. TiO_2 content ranges from 0.11 to 0.23 wt. %. Again, these are much lower contents than observed in the 11-15 cm section of the core, and this interval actually shows TiO_2 content increasing with increasing SiO_2 content. FeO and MgO contents range from 0.75 to 2.61 and 0.04 to 0.34 wt. %, respectively. MgO contents are again lower than those observed in the 11-15 cm section of the core. Mg# values range from 5.78 to 25.08. Na_2O and K_2O contents range from 3.57 to 4.72 wt. % and 1.32 to 3.00 wt. %, respectively. Total alkali content increases very slightly with increasing SiO_2 content. Al_2O_3 content ranges from 11.54 to 12.41 wt. %. Again, this is a smaller variance than in the 11-15 cm segment. These values increase with increasing SiO_2 content. Little to no Cr_2O_3, SO_3, and NiO are observed in these particles. Total content ranges from 94.55 to 100.64 wt. %. Trace element data were not obtained for this interval.

4.3.10 Interval 42-42.5 cm

The chemical composition of glass particles from this interval displays similar trends to those observed in intervals 41-41.5 cm and 41.5-42 cm. SiO_2 contents range from 69.78 to 76.91 wt. %. TiO_2 content ranges from 0.08 to 0.35 wt. %. These are low contents in relation to the 11-15 cm segment of the core, and TiO_2 contents here decrease with increasing SiO_2 content. FeO and MgO contents range from 1.33 to 4.88 and 0.05 to 0.60 wt. %, respectively. Again, MgO

contents are relatively lower than those observed in the 11-15 cm section of the core. Mg# values range from 3.34 to 37.88, which is expected for particles that originate from an evolved source. The Na_2O and K_2O contents range from 2.49 to 4.90 wt. % and 1.60 to 2.93 wt. %, respectively. There is no trend in total alkali content versus SiO_2 content for this interval. Al_2O_3 content ranges from 11.90 to 15.03 wt. %, and these values decrease with increasing SiO_2 content. Trace amounts of Cr_2O_3, SO_3, and NiO are observed in these particles. Total content ranges from 94.26 to 99.20 wt. %. Trace element data were obtained using SIMS for this interval. Grains display both positive and negative europium anomalies, and are relatively enriched in the LREEs in relation to the HREEs (Figure 7C).

4.3.11 Interval 43-43.5cm

Glass chemistry of the 43-43.5 cm interval displays similar trends to those observed in the other three intervals from this segment of the drill hole. SiO_2 contents range from 71.36 to 79.65 wt. %. TiO_2 content ranges from 0.07 to 0.30 wt. %. Again, these are relatively low contents in relation to the 11-15 cm segment. TiO_2 contents here decrease with increasing SiO_2 contents. FeO and MgO contents range from 0.12 to 2.53 and 0.00 to 0.42 wt. %, respectively. Mg# values range from below detection limit to 28.90. The Na_2O and K_2O contents range from 1.12 to 4.58 wt. % and 0.29 to 2.81 wt. %, respectively. Total alkali content increases with increasing SiO_2 content. Al_2O_3 content ranges from 10.59 to 14.25 wt. %, and these values decrease with increasing SiO_2 content. Insignificant amounts of Cr_2O_3, SO_3, and NiO are observed in these particles. Total content ranges from 92.82 to 100.27 wt. %, the largest variance observed so far in the 41-45 cm segment of core. Trace element data were not obtained for this interval.

4.3.12 Interval 43.5-44 cm

Glass geochemistry in this interval is similar to the other intervals examined from the 41-45 cm segment of core. SiO_2 contents range from 71.34 to 93.70 wt. %. This is the largest range in SiO_2 content observed in the 41-45 cm segment. TiO_2 content ranges from 0.09 to 0.56 wt. %. Here, TiO_2 contents decrease with increasing SiO_2 content. FeO and MgO contents range from 0.19 to 5.20 wt. % and below detection limit to 1.53 wt. %, respectively. Apart for the highest value, MgO contents are significantly lower than those observed in the 11-15 cm section of the core. Mg# values range from below detection limit to 34.47. The Na_2O and K_2O contents range from 1.48 to 4.58 wt. % and 0.10 to 2.73 wt. %, respectively. Total alkali content increases with increasing SiO_2 content, a trend that has been observed in multiple other intervals. Al_2O_3 content ranges from 9.86 to 12.85 wt. %, and Al_2O_3 content decreases with increasing SiO_2 content. Trace amounts of Cr_2O_3, SO_3, and NiO are present in these particles. Total content ranges from 95.72 to 100.19 wt. %. Trace element data were not obtained for this interval.

4.3.13 Interval 44-44.5 cm

The chemical composition of glass particles from this interval displays similar trends to those observed throughout the 41-45 cm segment of core. SiO_2 contents range from 65.49 to 81.77 wt. %. TiO_2 content ranges from 0.08 to 0.37 wt. %, and TiO_2 contents decrease with increasing SiO_2 content. FeO and MgO contents range from 0.26 to 4.55 and below detection limit to 2.33 wt. %, respectively. MgO contents, on average, for this interval are higher than other intervals within the 41-45 cm segment. Mg# values range from 0.00 to 47.72, the highest Mg# recorded so far for the 41-45 cm segment. The Na_2O and K_2O contents range from 3.41 to 4.87 wt. % and 0.27 to 2.36 wt. %, respectively. Again, total alkali content increases with increasing SiO_2 content. Al_2O_3 content ranges from 11.22 to 15.16 wt. % and decreases with increasing SiO_2 content. As with all other samples, trace, insignificant amounts of Cr_2O_3, SO_3,

and NiO are observed in these particles. Total content ranges from 96.17 to 100.87 wt. %. Overall, these are high totals in comparison to the other intervals observed both in the 11-15 cm and 41-45 cm segments. Trace element data were not obtained for this interval.

4.3.14 Interval 44.5-45 cm

Again, it is observed that the geochemical variation in this interval is not as pronounced as in intervals within the 11-15 cm segment. SiO_2 contents range from 70.72 to 86.82 wt. %. TiO_2 content ranges from 0.07 to 0.65 wt. %. These contents are similar to what has been observed in both the 11-15 cm and 41-45 cm segments, and TiO_2 content tends to decrease with increasing SiO_2 content. FeO and MgO contents range from 0.17 to 3.68 and below detection limit to 0.51 wt. %, respectively. Apart from the highest content value recorded in this interval, MgO contents are relatively low in comparison to both the 11-15 cm segment and other intervals of the 41-45 cm segment. Mg# values range from below detection limit to 21.70. These are, on average, the lowest observed Mg#s in both core segments. The Na_2O and K_2O contents range from 1.90 to 5.86 wt. % and 0.30 to 2.49 wt. %, respectively. Total alkali content increases with increasing SiO_2 content. Al_2O_3 content ranges from 8.19 to 18.17 wt. %, the largest range in Al_2O_3 content observed in the 41-45 cm segment thus far. Almost no Cr_2O_3, SO_3, and NiO are observed in these particles. Total content ranges from 90.14 to 100.82 wt. %. This is the largest range in total value for the 41-45 cm segment. Trace element data was obtained using SIMS for this interval. Grains display negative europium anomalies, and are slightly more enriched in the LREEs in relation to the HREEs (Figure 7D).

Figure 7A | REE Plot: Interval 13.5-14 cm

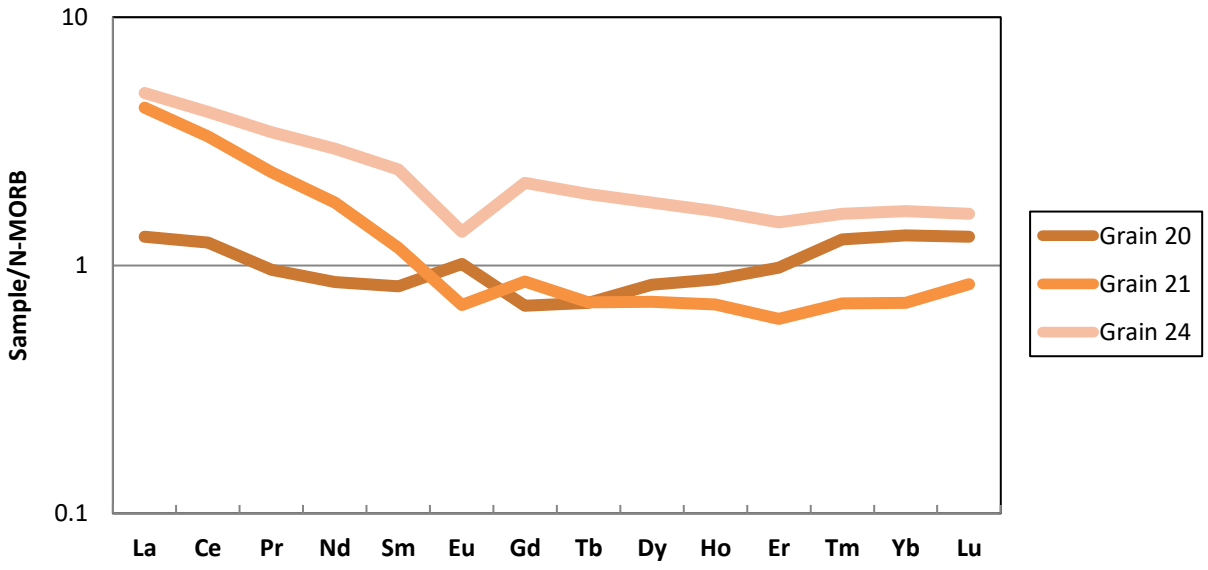

Figure 7B | REE Plot: Interval 14.5-15 cm

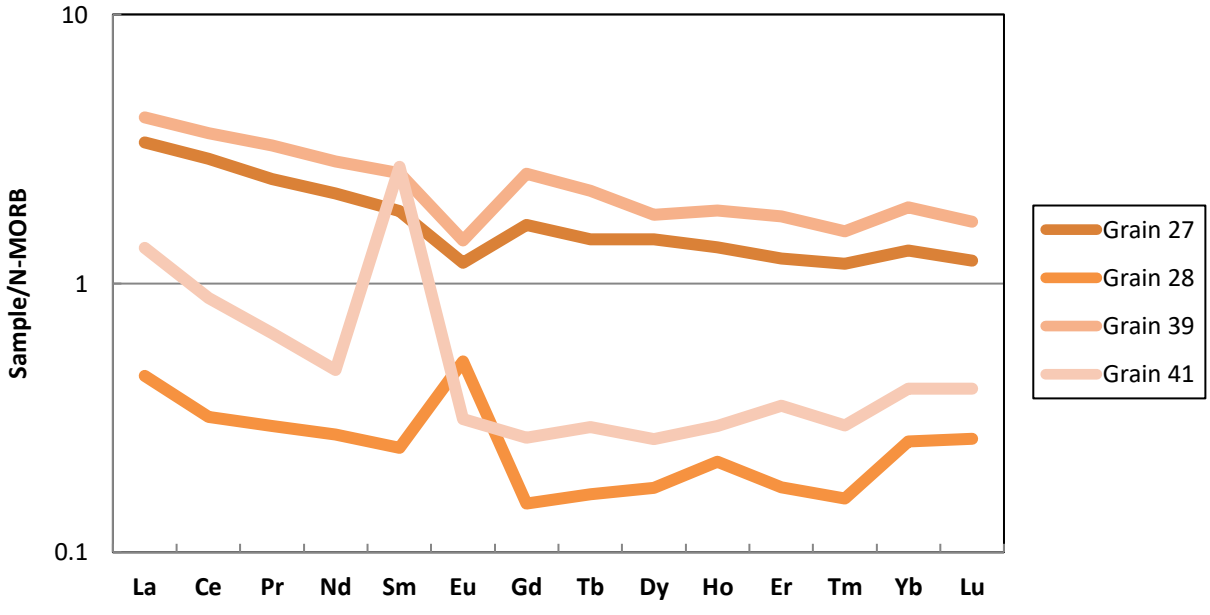

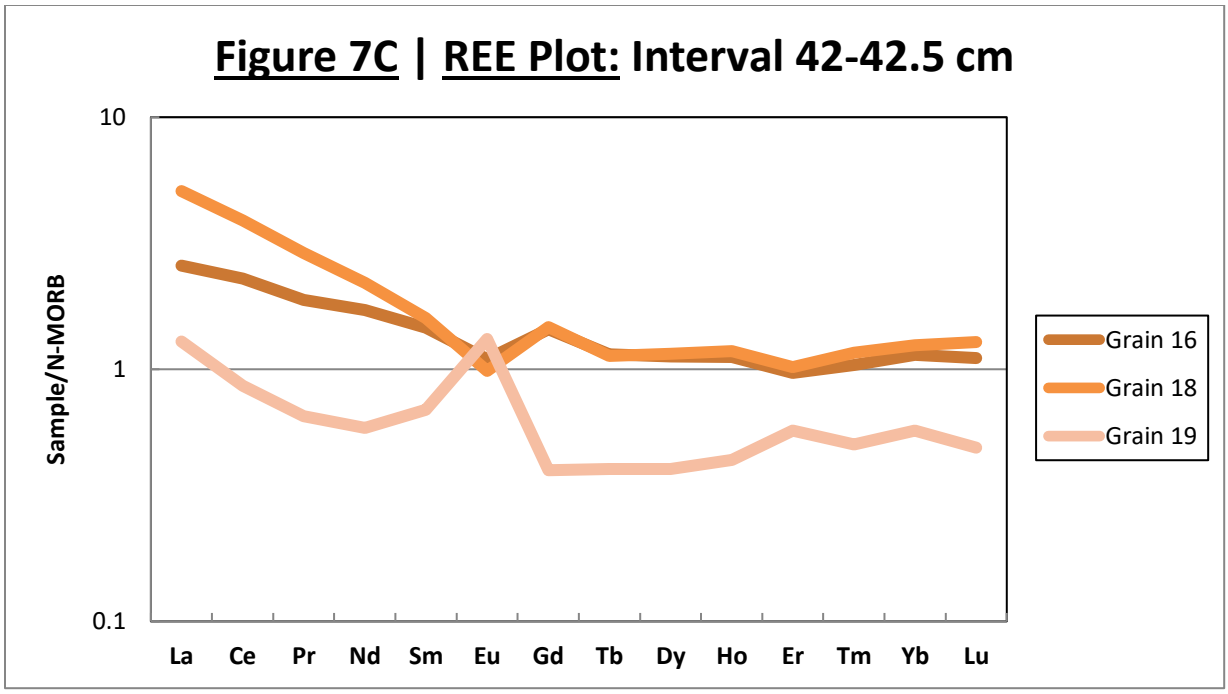

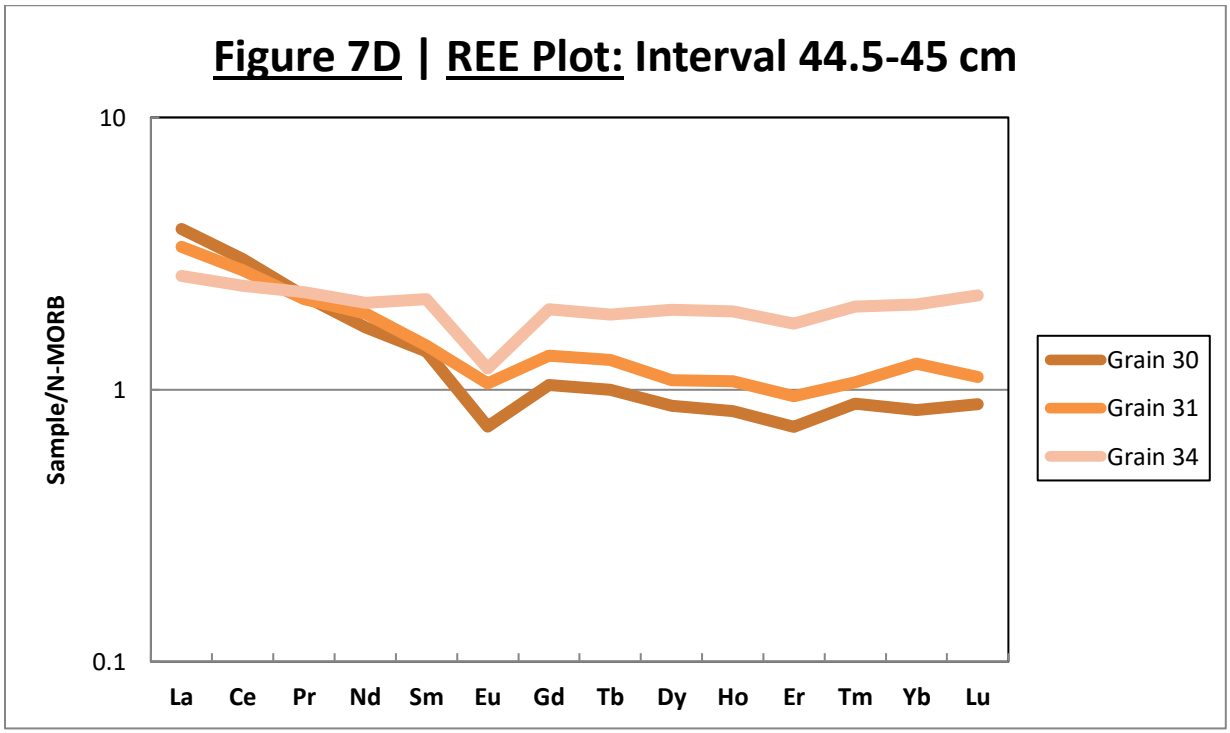

Figure 7A-D. REE plots where the data obtained from each grain analyzed (each element ratioed to ^{30}Si, normalized to typical N-MORB) is plotted on a logarithmic line graph. Normalization values are obtained from Sun & McDonough (1989).

5 | DISCUSSION

5.1 Eruptive Conditions

The overall composition of the > 45 μm, non-calcareous material of both the 11-15 cm and 41-45 cm segments of core U1396-1H-4W suggests that both deposits were generated from explosive eruptions. The most common particle types observed in all intervals were white glass/mineral and vesicular pumice, the latter of which is primarily generated in andesitic to rhyolitic, explosive systems. Plagioclase and quartz crystals (white mineral) can be found in tephra deposits that were formed from both explosive and effusive eruptions, but these deposits would contain significantly more scoria had they been generated by an effusive, mafic eruption. These interpretations made from point counting were confirmed by the high silica content of glasses observed throughout all intervals of both the 11-15 cm and 41-45 cm segments of the core.

The variance in composition and crystallinity between the 11-15 cm and 41-45 cm segments of the core can be interpreted as due to different eruptive conditions (Figures 5A-C). Eruptive material that is high in total alkali content and high in SiO_2 content is assumed to be the most evolved product of an explosive, Vulcanian eruption. During Vulcanian explosions, material from the uppermost several hundred meters of the ascending magma body is ejected on a timescale of less than a few minutes, making it impossible to crystallize completely (Harford et. al., 2003). In contrast, eruptive material with the lowest total alkali content is expected to be generated from the lowermost several hundred meters of the conduit, as it would be the least chemically evolved (Sparks et al., 1998). A difference in total alkali content versus SiO_2 content (wt. %) is most pronounced in the 11-15 cm segment of the core. This could be the result of several different processes taking place in the magma chamber.

The first and most obvious process to examine is a similar one that led to the 1995-1998 eruption of the SS-SH volcanic complex: a magma mixing process in which a more mafic body intruded into a more geochemically evolved magma chamber. Devine et. al. (1998) examined the compositional variability of different minerals associated with the 1995-1998 eruption, drawing particular attention to large differences in composition observed in magnetite crystals. While magnetite crystals tend to form under more stable conditions than glass particles (which are quenched upon eruption and do not have a defined crystallographic structure), it is possible that the compositional variability of the 11-15 cm segment could be attributed to an eruption that was triggered by magma mixing processes. If mixing had been occurring over a short period of time in the magma chamber, it would make sense that the particles erupted would show evidence of a less evolved magma and would trend to a more andesitic final composition.

The second process that could result in compositional variability in the 11-15 cm segment could be that a highly accelerated rate of magma ascension impeded the degassing of magma as it rose. If a magma is ascending through the conduit at such a fast rate that it cannot de-gas significantly, the magma will also not fractionate significantly, ultimately erupting material that displays a wide variety of compositions, some evidencing a more primitive magma source. (Such an eruption would therefore produce a deposit that would be difficult to interpret, considering the wide variation in geochemical data.) This hypothesis is supported by Harford et. al. (2003), another study on the 1995-1998 eruption, which concluded that that variation in matrix glass composition of pumice clasts indicates that shallow-level processes dominated degassing in the most recent eruption.

The eruptive material preserved in the 41-45 cm segment of core apparently was erupted in a somewhat different nature than the material from the 11-15 cm segment. As evidenced in all

intervals of the 41-45 cm segment, there is relatively less compositional variability in the glass particles in comparison to the 11-15 cm segment, and almost all glasses can be classified as rhyolitic. This suggests that the magma feeding this eruption had been evolving and fractionating within the magma chamber over longer periods of time. The 11-15 cm core segment does contain some glass particles that suggest a magma source of more primitive nature, but overall the variation in SiO_2, total alkali, CaO, Mg#, and other chemical constituents are not great enough to definitively conclude that the pre-eruptive conditions preserved in glasses from the 41-45 cm segment of core were significantly different. The more likely hypothesis is that the magma ascended up through the crustal column at a slower rate than that which generated 11-15 cm glasses. This process would have allowed for the magma to fractionate out minor amounts of more primitive minerals and material as it rose through the conduit. Upon eruption, the magma would have quenched into glass particles which were not only more evolved than the one from the 11-15 cm core section, but also more homogeneous in composition.

Unfortunately, the trace element data obtained for these samples is inconclusive considering the relatively low amount of analyses performed and contradictory features of the data. For example, the negative Europium anomaly (coupled with enrichment in LREE) is typical of plagioclase, which indicates that part of a plagioclase grain may have been sputtered during analysis, thus yielding inaccurate results. However, the enrichment in LREE relative to HREE is indicative of a relatively evolved and fractionated melt, which confirms the hypotheses proposed after analyzing the electron microprobe data. In the future, different analytical methods should be considered in order to obtain more accurate trace element data. For example, the separated material should be re-melted and quenched into a glass pill so that the spot size used for analysis can be larger and returns in counts-per-second can be greater.

5.3 Comparison to Past Work on the 1995-1998 eruption at SS-SH

This study has already visited past experimental and geochemical studies on volcanics from the SS-SH volcanic complex, the results of which have suggested that the most recent eruption was triggered by the mixing of magmas of two different compositions. This feature can also apparently be attributed to the varying composition of glass particles observed in core segment 11-15 cm (Devine et al., 1998). The hypothesis was proposed that a more mafic magma intruded into an andesitic magma chamber, triggering magma mixing that caused the 1995 eruption. This idea is supported by the large compositional variability of magnetite crystals, the high-Mg# rims of orthopyroxene grains, the An-rich rims on plagioclase phenocrysts, and the scalloped textures of hornblende crystals (Devine et al., 1998). These features all indicate that a heating event raised the temperature of the magma to the reaction boundary at which hornblende reacts to form clinopyroxene plus melt, which accounts for the scalloped textures at hornblende-clinopyroxene reaction boundaries and rims on both orthopyroxene and plagioclase (Rutherford & Devine, 1988; Barclay et al., 1998). In addition, the recent eruption was largely extrusive, except for ash venting episodes and a few episodes of Vulcanian explosive eruptions (Devine et al., 2003). These features could also be attributed to a faster ascension rate of the magma through the crustal column (Harford et al., 2003).

This study is inherently different from those of Sparks, Devine, and Rutherford, however, in that they were sampling and studying mineral and whole rock compositions from on-land deposits related to the explosive 1995-1998 eruption, detailing both their textural and compositional variations. In contrast, this study examines only the glass particles associated with cryptotephra deposits, which are expected to represent quenched melts of eruptive material from smaller, potentially dome-forming eruptions. Figure 8 shows the differences observed in the

results of this study compared to several studies on volcanic material (whole rock and matrix glass) from the 1995-1998 eruption.

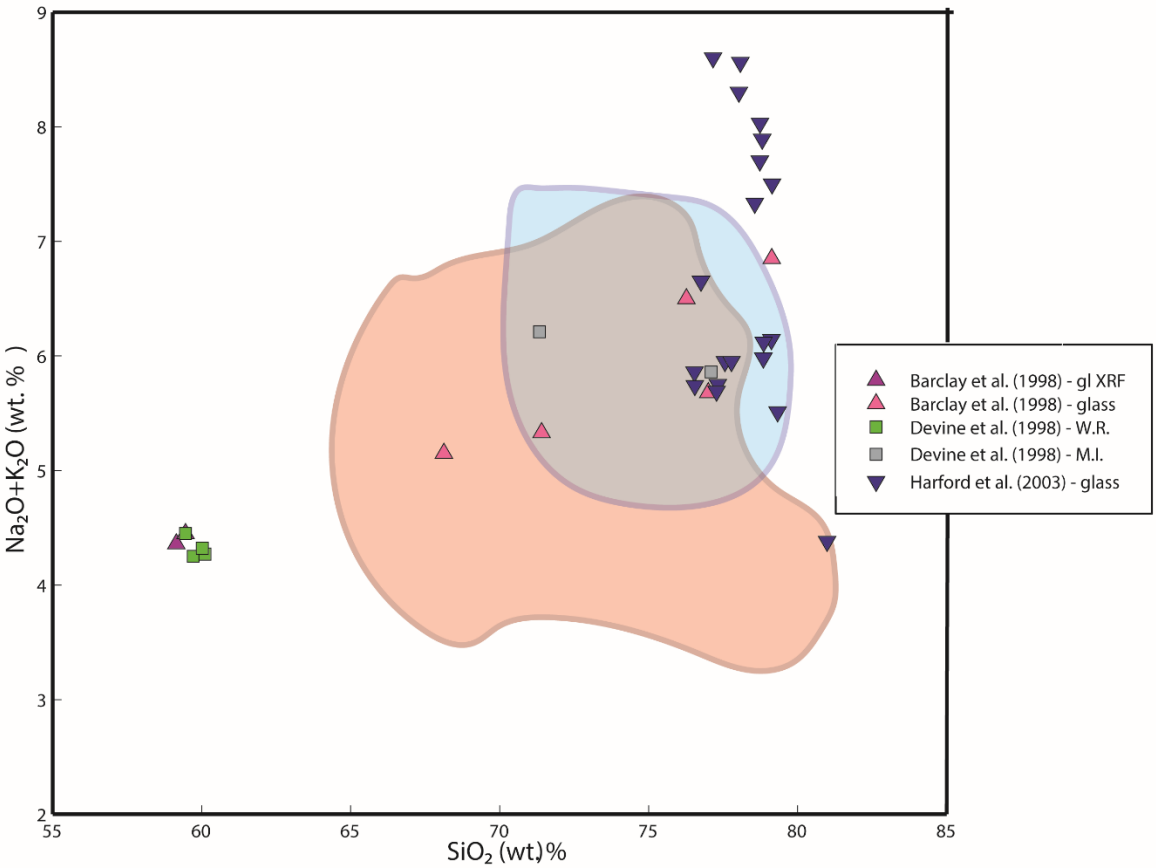

Figure 8. TAS (Total Alkali Silica) diagram showing the compositional regions which glass particles from the 11-15 cm (red) and 41-45 cm (blue) core segments occupy. Data on glass particles, whole rocks, and melt inclusions generated by the 1995-1998 are plotted on the same diagram, displaying a similar average igneous trend than the data from this study.

The results of this study demonstrate that glass particles in the two cryptotephra samples are similar in geochemistry to the SS-SH volcanic complex (and the associated magma storage region), indicating that there has not been significant geochemical evolution over the past ~400,000 years. But, a comparison to studies from the 1995-1998 eruptions can provide some insight into the processes by which magma is brought from the chamber to the surface, which are likely not uniform over each eruptive event. Figure 7 shows this geochemical evolution by comparing various matrix glass compositions to the compositions obtained in this study. Rutherford & Devine (2003), Barclay et al. (1998), and Harford et al. (2003) all observe matrix glass compositions similar to those observed in the 41-45 cm and 11-15 cm sections of the core, but compositions in some of the glasses observed in segment 11-15 cm have not been documented in these other studies on the recent volcanic history of SS-SH.

This is significant because it provides evidence that the processes associated with the eruption preserved in segment 11-15 cm are indeed different than those observed both in the 41-45 cm segment and the 1995 SS-SH eruption. This study has demonstrated that compositional variations in glasses from this segment are associated with either magma mixing or an accelerated ascension rate through the conduit. The compositional variation of minerals associated with the 1995-1998 eruption is primarily understood to be the result of magma mixing and ascension rate (Devine et. al., 1998). However, the kind of compositional variation observed in glasses is not a change in SiO_2 content, but rather a change in other major element compositions, such as Na_2O and K_2O (Harford et. al., 2003). The eruptive material preserved in the segment 11-15 cm also shows a significant variation in both SiO_2 and total alkali content, unlike the 1995-1998 eruption. Therefore, it can be assumed that the volcanic eruption preserved in the 11-15 cm segment is affected even more significantly by either magma mixing or

accelerated ascension rates. In this case, there could have been a more mafic magma being fed into the magma chamber, or the ascension rate could have been even faster than the one observed in 1995-1998. However, it is most likely that the compositional variation of the 11-15 cm core segment is due to accelerate ascension rate, because there is a relative depletion of black minerals and black glass in comparison to the amounts of white glass and white minerals. Were magma mixing the more likely process, there would be significantly more black glass/mineral and scoria observed in point counting results, and the TAS diagram would likely show data points that plot in the basalt region. Although, it is possible that mixing of an andesitic and silicic magma occurred.

5.4 Comparison to Past Work on Centre Hills and Silver Hills volcanic complexes

Temporally, it makes sense that the two cryptotephra deposits from this study would most likely have been generated by the Centre Hills volcanic complex, considering it was still active around 400,000 years ago. Therefore, the eruptive material from this study is compared to the whole rock pumice compositions that were analyzed by Coussens et al. (2017) from the 0.6 Ma – 0.4 Ma eruptive period for Centre Hills (Figure 9).

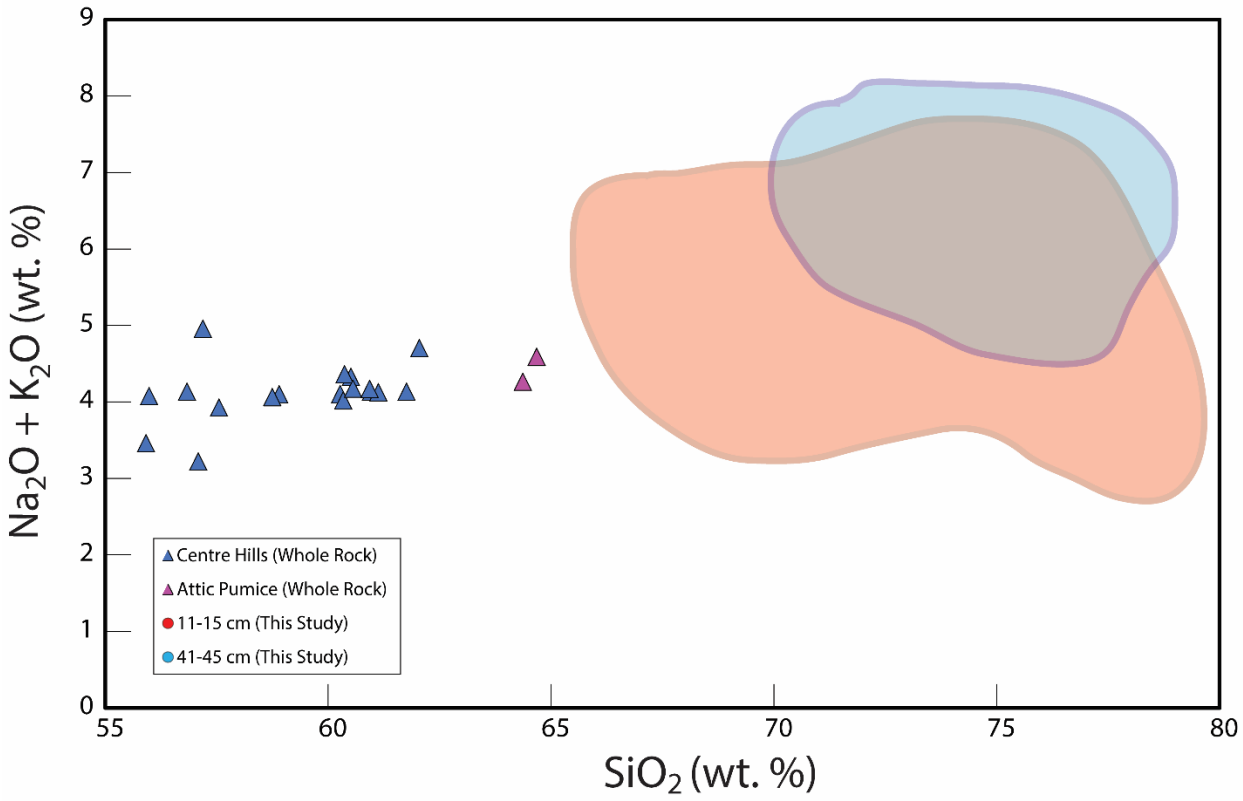

Figure 9. TAS (Total Alkali Silica) Diagram showing the values of SiO_2 (wt. %) vs. $NaO + K_2O$ (wt. %) for the 11-15 cm and 41-45 cm core segments, along with the whole rock data from Coussens et al. (2017). The average trend for data from both studies is an increase in total alkali content as silica increases, with the glass particles from this study appearing significantly more evolved than both the Attic Pumice and other tephra deposits comprising Centre Hills eruptive material.

Figure 9 displays the data from this study along with the data from Coussens et al., (2017). My data fit almost perfectly on a linear trendline with the whole rock pumice analyses from Centre Hills (the Attic Pumice is shown in peak, as it was previously concluded by Coussens et al. (2017) to be the most evolved volcanic deposit associated with Centre Hills). However, the samples from this work appear to be more evolved than the material from the Attic Pumice layer. This could be due to the fact that analyses from this study were performed on microcrystalline glass particles rather than a larger slab of pumice. However, Coussens et al. (2017) note that the Attic Pumice should be the last explosive eruption from this second eruptive cycle of Centre Hills, at around 400,000 years ago., and the cryptotephra deposits from this study are from an almost identical time period. Therefore, it is possible that my samples represent an eruptive event at Centre Hills which generated material more evolved than the Attic Pumice. This material could have been overlooked in the past due to the difficulty in identifying cryptotephra layers, but it is also possible that small, effusive, dome-forming eruptions continued even after the massive eruption that produced the Attic Pumice.

Nevertheless, the trend in evolution between this study and the 2017 Coussens et al. study appears to be quite similar. Therefore, the cryptotephra deposits from this study are more likely associated with the Centre Hills volcanic complex than the SS-SH volcanic complex, due to the correlation between the age of the eruptive material from this study and that of previously documented Centre Hills volcanic material, and the correlation between the average igneous trends of the eruptive material from this study and that of Coussens et al. (2017).

5.5 Cryptotephra from U1396-1H-4W on a global scale

The average glass composition of core segments 11-15 cm and 41-45 cm is plotted in a TAS diagram along with average glass compositions from other eruptions on convergent margins

in recent history (1800 CE-present). This relationship is illustrated in Figure 10. The most prominent relationship observed is that, on average, eruptive material from these prehistoric SS-SH eruptions is depleted in total alkali content relative to modern day eruptions. It's difficult to make a conclusion as to what this trend means, but it's possible that the difference in alkali content of the cryptotephra units (11-15 cm and 41-45 cm) and the eruptive material of explosive eruptions from the 19th, 20th, and 21st centuries is due to the difference in eruptive conditions. All of the eruptive material to which the cryptotephra from this study is compared was generated during a large, explosive eruption.

The massive, explosive eruptions that scientists associate with stratovolcanoes are often the most studied and well-documented volcanic deposits. This is true for several reasons. (1) Massive, explosive eruptions trigger a short-lived scientific interest in better understanding how these explosive eruptions function in order to be better prepared for future eruptions. (2) The eruptive material from explosive eruptions is more readily available for scientists to study (as more of it is generated), whereas cryptotephra and other thin deposits from effusive eruptions can become disturbed more easily by chemical weathering or surficial erosion processes. While it is important to understand how these explosive eruptions function and how the magma storage regions associated with them evolve, only studying these kinds of eruptions can create a biased view of how volcanic complexes work and how magma chambers evolve.

Explosive eruptions only make up about 20-30 % of a volcano's eruptive cycle, whereas the other 70-80 % are effusive, dome-forming eruptions that leave behind very thin, often undetectable deposits, like cryptotephra (Crisp, 1984). Therefore, studying only the explosive eruptions creates a biased view of how volcanic systems function across Earth. One theory about the cryptotephra deposits being slightly more depleted in alkalis than the explosive eruptive

material is that lower alkali contents in magmas are associated with more effusive eruptions than explosive ones. If this is true, then it should be observed that as more and more effusive eruptions occur within a single volcanic complex, we should see the geochemistry of associated deposits display a slighter enrichment in alkalis over time, until the system reaches a threshold where an explosive eruption occurs. The threshold is generally determined by the buildup of volatiles in the system; therefore, it is possible that volatiles are building up in the magma chamber as fractionation progresses, which is then responsible for causing a more explosive eruption. If this is true, an overall increase in total alkalis would be observed too.

Figure 10 demonstrates that there is a significant difference in the total alkali and silica content of tephra/lithologic deposits associated with major, explosive eruptions and those associated with effusive, dome-forming eruptions. The difference in total alkali content is especially pronounced, with the more geochemically evolved data points being associated with the more explosive, Vulcanian eruptions. On average, the data from this study trends towards lower total alkali content, which is unexpected for effusive material. The trend is typically the other way around. Material that is involved in effusive eruptions has generally spent longer in shallow magma chambers, allowing degassing to occur, thereby generating an effusive, rather than explosive, eruption. During the time in the shallow chamber the magma further fractionates, driving the alkali content up (Harford et al., 2003).

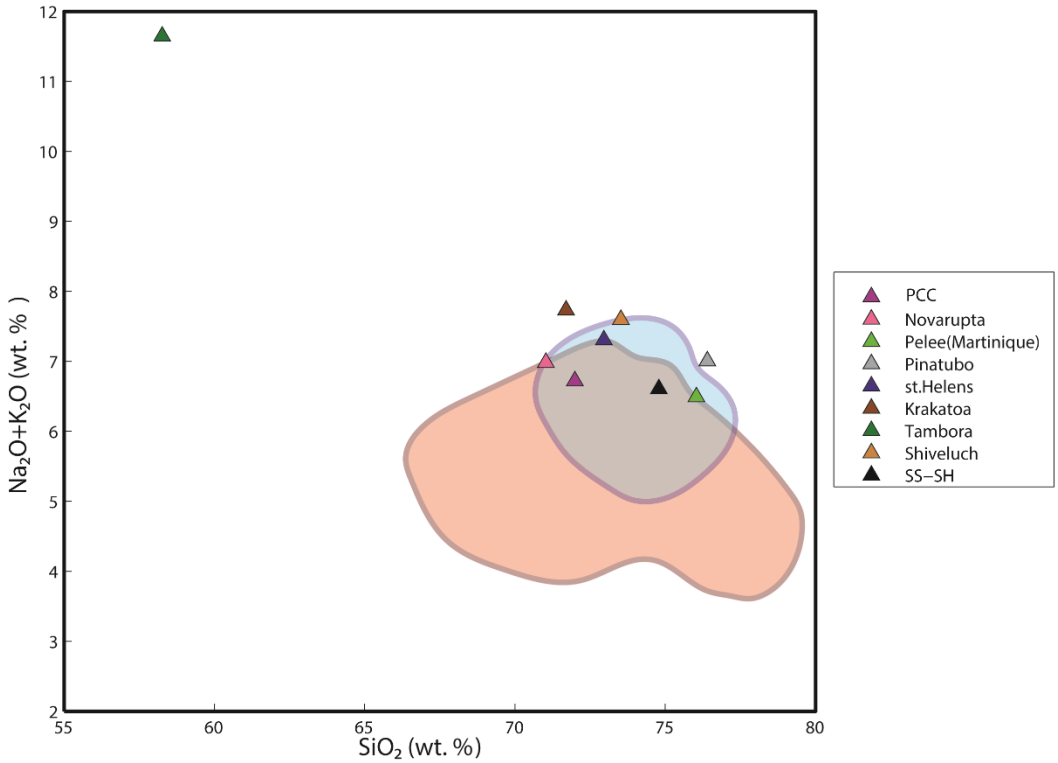

Figure 9. TAS (Total Alkali Silica) Diagram showing the regions that are compositionally occupied by data from both the 11-15 cm (red) and 41-45 cm (blue) segments of the core. Explosive eruptions (from the past three centuries) that have been extensively studied, tend to contain relatively more total alkalis than the cryptotephra deposits examined in this study. I used datasets from the following volcanoes: Puyehue Cordon Caulle (Castro et al., 2013), Novarupta (Hammer et al., 2002), Pelee (Martel et al., 1998), Pinatubo (Rutherford & Devine, 1996), St. Helens (Rutherford et al., 1985), Krakatoa (Mandeville et al., 1996), Tambora (Gertisser et. al., 2011), Shiveluch (Ponomareva et al., 2007), and SS-SH (Harford et al., 2003).

6 | CONCLUSIONS

This study paves the way for a better understanding of the complex history associated with the island of Montserrat at its various volcanic complexes, in addition to other volcanoes in the Lesser Antilles Arc which share similar eruptive properties to Silver Hills, Centre Hills, and SS-SH. The extensive collection of cores retrieved from this IODP mission will allow for the study of eruptions previously unknown for all the volcanic complexes on Montserrat and may even provide geologists with a better understanding of how island arc volcanic systems evolve on the scale of 1 to 10 million years.

Physical and geochemical tests performed on glass particles associated with two different cryptotephra layers provide information about how volcanic activity on Montserrat has evolved from the Pliocene to the present day. The following conclusions summarize the results of this study:

- The amount and composition of physical material ejected from Montserrat's SS-SH volcanic complex varies slightly over time, but the same types of volcanic particles are observed in similar amounts across all eruptive material.
- The glass geochemistry of the two cryptotephra deposits (core segment 11-15 cm and 41-45 cm) is different, and slightly different geochemical trends occur in each interval. However, the overall composition of glass particles is primarily rhyolitic to slightly dacitic and andesitic.
- The variation in composition of glass particles in core segment 11-15 cm can be attributed to one of two processes:
    - Mixing of a more silicic and a more mafic magma in the chamber which feeds the volcanic complexes on Montserrat, at around the same time as the eruption.

    - Relatively fast ascension rate of magma through the crustal column which leads to relatively less degassing until the magma reaches a subaerial environment. This is the more likely process, as relatively little black glasses/minerals were point-counted.

- The low variation in composition of glass particles in core segment 41-45 cm suggests that the magma either ascended through the conduit at a slower rate and degassed as it rose, or that the magma chamber fractionated significantly before the eruption
- The two cryptotephra deposits from this study are most likely associated with the Centre Hills volcanic complex on Montserrat. That is because they are similar in age to other eruptive material from Centre Hills, and they display an average igneous trend similar to older eruptive material from Centre Hills.
- The relatively low total alkali content of the cryptotephroic glass particles might suggest that effusive eruptions tend to have lower alkali contents than explosive ones, but this is really the other way around (Harford et al., 2003).
- The magma chamber which feeds Silver Hills, Centre Hills, and SS-SH does not evolve that significantly over the course of 400,000 years.
- More work is necessary in order to understand the complex volcanic history associated with the three volcanic complexes on Montserrat, and volcanic complexes across Earth (including other tectonic boundaries, as well). While the two cryptotephra layers examined in this study provide results important to understanding volcanic processes associated with the Centre Hills volcanic complex, these results certainly cannot be applied to every single volcanic complex in an island arc.

7 | REFERENCES CITED

Barclay, J., Rutherford, M.J., Carroll, M.R, Murphy, M.D., Devine, J.D., Gardner, J., Sparks, R.S.J., 1998, Experimental phase equilibria constraints on pre-eruptive storage conditions of the Soufriere Hills magma: Geophysical Research Letters, v. 25, p. 3437-3440

Blockley, S., Pyne-O'Donnell, S., Lowe, J., et al., 2005, A new and less destructive laboratory procedure for the physical separation of distal glass tephra shards from sediments: Quaternary Science Reviews, v. 24, no. 16, p. 1952-1960.

Cassidy, M., Trofimovs, J., Palmer, M.R., Talling, P.J., Watt, S.F.L., Moreton, S.G., and Taylor, R.N., 2013, Timing and emplacement dynamics of newly recognised mass flow deposits at ~ 8–12 ka offshore Soufrière Hills volcano, Montserrat: How submarine stratigraphy can complement subaerial eruption histories: Journal of Volcanology and Geothermal Research, v. 253, no. 0, p. 1-14.

Cassidy, M., Watt, S.F.L., Palmer, M.R., Trofimovs, J., Symons, W., Maclachlan, S.E., and Stinton, A.J., 2014, Construction of volcanic records from marine sediment cores: A review and case study (Montserrat, West Indies): Earth-Science Reviews, v. 138, no. 0, p. 137-155.

Castro, J.M., Schipper, C.I., Mueller, S.P., Militzer, A.S., Amigo, A., Parejas, C.S., Jacob, D., 2013, Storage and eruption of near-liquidus rhyolite magma at Cordón Caulle, Chile: Bulletin of Volcanology, v. 75.4, p. 702

Crisp, J. A., 1984, Rates of magma emplacement and volcanic output. Journal of Volcanology and Geothermal Research, v. 20, p. 177-211.

Coussens, M., Cassidy, M., Watt, S. F., Jutzeler, M., Talling, P. J., Barfod, D., & Palmer, M. R., 2017, Long-term changes in explosive and effusive behaviour at andesitic arc volcanoes: Chronostratigraphy of the Centre Hills Volcano, Montserrat. Journal of Volcanology and Geothermal Research, v. 333, p. 15-35.

Devine, J.D., Murphy, M.D., Rutherford, M.J., Barclay, J., Sparks, R.S.J., Carroll, M.R., Young, S.R., Gardner, J.E., 1998, Petrologic evidence for pre-eruptive pressure-temperature conditions, and recent reheating, of andesitic magma erupting at the Soufriere Hills Volcano, Montserrat, W.I.: Geophysical Research Letters, v. 25, p. 3669-3672

Devine, J.D., Rutherford, M.J., Norton, G.E., Young, S.R., Magma Storage Region Processes Inferred from Geochemistry of Fe-Ti Oxides in Andesitic Magma, Soufrière Hills Volcano, Montserrat, W.I.: Journal of Petrology, v. 44, p. 1375-1400

Ewert, J.W., and Miller, C.D., 1995, The USGS/OFDA Volcano Disaster Assistance Program: Open-File Report Report 95–553, http://pubs.er.usgs.gov/publication/ofr95553.

Expedition 340 Scientists, 2012, Lesser Antilles volcanism and landslides: implications for hazard assessment and long-term magmatic evolution of the arc: IODP Prel. Rept., 340

Fisher, E.A., 2015, Evaluating Reflectance Spectroscopy as a Method of Rapid Cryptotephra Identification: Tephrochronology Of the Lesser Antilles Arc: Tufts University. Digital Collections and Archives, p. 1-44

Fraass, A. J., Wall-Palmer, D., Leckie, R. M., Hatfield, R. G., Burns, S. J., Le Friant, A., & Palmer, M., 2016, A revised Plio-Pleistocene age model and paleoceanography of the northeastern Caribbean Sea: IODP Site U1396 off Montserrat, Lesser Antilles: Stratigraphy, v. 13, p. 183-203.

Garmon, W. T., Allen, C. D., & Groom, K. M., 2017, Geologic and Tectonic Background of the Lesser Antilles. In Landscapes and Landforms of the Lesser Antilles, Springer Cham., p. 7-15

Gertisser, R., Self, S., Thomas, L. E., Handley, H. K., Van Calsteren, P., & Wolff, J. A., 2011, Processes and timescales of magma genesis and differentiation leading to the great Tambora eruption in 1815. Journal of Petrology, v. 53, p. 271-297.

Hammer, J. E., Rutherford, M. J., & Hildreth, W., 2002, Magma storage prior to the 1912 eruption at Novarupta, Alaska: Contributions to Mineralogy and Petrology, v. 144, p. 144-162.

Harford, C. L., Pringle, M. S., Sparks, R. S. J., & Young, S. R., 2002, The volcanic evolution of Montserrat using $^{40}Ar/^{39}Ar$ geochronology: Geological Society, London, Memoirs, v. 21(1), p. 93-113.

Harford, C.L., Sparks, R.S.J, Fallick, A.E., 2003, Degassing at the Soufrière Hills Volcano, Montserrat, Recorded in Matrix Glass Compositions: Journal of Petrology, v. 44, p. 1503-1523

Hatter, S. J., Palmer, M. R., Gernon, T. M., Taylor, R. N., Cole, P. D., Barfod, D. N., & Coussens, M., 2018, The evolution of the Silver Hills volcanic center, and revised $^{40}Ar/^{39}Ar$ geochronology of Montserrat, Lesser Antilles, with implications for island arc volcanism: Geochemistry, Geophysics, Geosystems, v. 19(2), p. 427-452.

Le Friant, A., Lock, E., Hart, M., et al., 2008, Late Pleistocene tephrochronology of marine sediments adjacent to Montserrat, Lesser Antilles volcanic arc: Journal of the Geological Society, v. 165, no. 1, p. 279-289.

Lowe, D.J., 2011, Tephrochronology and its application: a review: Quaternary Geochronology, v. 6, no. 2, p. 107-153.

Mandeville, C. W., Carey, S., & Sigurdsson, H., 1996, Magma mixing, fractional crystallization and volatile degassing during the 1883 eruption of Krakatau volcano, Indonesia. Journal of Volcanology and Geothermal Research, v. 74, p. 243-274.

Martel, C., Pichavant, M., Bourdier, J. L., Traineau, H., Holtz, F., & Scaillet, B., 1998, Magma storage conditions and control of eruption regime in silicic volcanoes: experimental evidence from Mt. Pelée: Earth and Planetary Science Letters, v. 156, p. 89-99.

McCanta, M.C., Hatfield, R.G., Thomson, B.J., Hook, S.J., Fisher, E.A, 2015, Identifying cryptotephra units using correlated rapid, nondestructive methods: VSWIR spectroscopy, X-ray, fluorescence, and magnetic susceptibility: Geochemistry, Geophysics, Geosystems, v. 16, p. 4029-4056

Ponomareva, V., Portnyagin, M., Pevzner, M., Blaauw, M., Kyle, P., & Derkachev, A., 2015, Tephra from andesitic Shiveluch volcano, Kamchatka, NW Pacific: chronology of explosive eruptions and geochemical fingerprinting of volcanic glass: International Journal of Earth Sciences, 104(5), 1459-1482.

Robertson, R., Cole, P., Sparks, R.S.J., Harford, C., Lejeune, A.M., McGuire, W.J., Miller, A.D., Murphy, M.D., Norton, G., Stevens, N.F., Young, S.R., 1998, The explosive eruption of Soufriere Hills Volcano, Montserrat, West Indies, 17 September, 1996: Geophysical Research Letters, v. 25, p. 3429-3432

Rutherford, M. J., & Devine, J. D., 1996, Preeruption pressure-temperature conditions and volatiles in the 1991 dacitic magma of Mount Pinatubo: Fire and mud: eruptions and lahars of Mount Pinatubo, Philippines, p. 751-766.

Rutherford, M.J., Devine, J.D., Barclay, J., 1998, Changing Magma Conditions and Ascent Rates during the Soufriere Hills Eruption on Montserrat: GSA Today, v. 8, p. 1-7

Rutherford, M.J., Devine J.D., 2003, Magmatic Conditions and Magma Ascent as Indicated by Hornblende Phase Equilibria and Reactions in the 1995-2002 Soufrière Hills Magma: Journal of Petrology, v. 44, p. 1433-1454

Rutherford, M. J., Sigurdsson, H., Carey, S., & Davis, A., 1985, The May 18, 1980, eruption of Mount St. Helens: 1. Melt composition and experimental phase equilibria: Journal of Geophysical Research: Solid Earth, v. 90, p. 2929-2947.

Sparks, R.S.J., Young, S.R., Barclay, J., Calder, E.S., Cole, P., Darroux, B., Davies, M.A., Druitt, T.H., Harford, C., Herd, R., James, M., Lejeune, A.M., Loughlin, S., Norton, G., Skerrit, G., Stasiuk, M.V., Stevens, N.S., Toothill, J., Wadge, G., Watts, R., 1998, Magma production and growth of the lava dome of the Soufriere Hills volcano, Montserrat, West Indies: November 1995 to December 1997: Geophysical Research Letters, v. 25, p. 3421-3424

Sun, S. S., & McDonough, W. S., 1989, Chemical and isotopic systematics of oceanic basalts: implications for mantle composition and processes: Geological Society, London, Special Publications, v. 42, p. 313-345.

Trofimovs, J., Foster, C., Sparks, R., et al., 2012, Submarine pyroclastic deposits formed during the 20th May 2006 dome collapse of the Soufrière Hills Volcano, Montserrat: Bulletin of Volcanology, v. 74, no. 2, p. 391-405.

Trofimovs, J., Amy, L., Boudon, G., et al., 2006, Submarine pyroclastic deposits formed at the Soufrière Hills volcano, Montserrat (1995–2003): What happens when pyroclastic flows enter the ocean?: Geology, v. 34, no. 7, p. 549-552.

Trofimovs, J., Talling, P.J., Fisher, J.K., et al., 2013, Timing, origin and emplacement dynamics of mass flows offshore of SE Montserrat in the last 110?ka: Implications for landslide and tsunami hazards, eruption history, and volcanic island evolution: Geochemistry, Geophysics, Geosystems, v. 14, no. 2, p. 385-406.

United Kingdom Foreign and Commonwealth Office, 2018, Montserrat: Montserrat Travel Advice, www.gov.uk/foreign-travel-advice/montserrat

Wall-Palmer, D., Coussens, M., Talling, P. J., Jutzeler, M., Cassidy, M., Marchant, I., ... & Hart, M. B., 2015, Late Pleistocene stratigraphy of IODP Site U1396 and compiled chronology offshore of south and south west Montserrat, Lesser Antilles: Geochemistry, Geophysics, Geosystems, v. 15, p. 3000-3020.

Williams, P., 1985, Secondary ion mass spectrometry: Annual Review of Materials Science, v. 15.1, p. 517-548.

Zalm, P. C., 1994, Secondary ion mass spectrometry: Vacuum, v. 45, p. 753-772

Zellmer, G. F., Sparks, R. S. J., Hawkesworth, C. J., & Wiedenbeck, M., 2003, Magma emplacement and remobilization timescales beneath Montserrat: insights from Sr and Ba zonation in plagioclase phenocrysts. Journal of Petrology, v. 44, p. 1413-1431.

8 | APPENDICES

8.1 Appendix A: Pount Counting Results

Table 1 Component analysis for core segment 11-15cm

Core	U1396C-1H-4W		U1396C-1H-4W		U1396C-1H-4W		U1396C-1H-4W	
Segment of interest (cm downcore)	11-15cm		11-15cm		11-15cm		11-15cm	
Subsection sampled (cm downcore)	11-11.5cm		11.5-12cm		12-12.5cm		12.5-13cm	
cm^3 of material disaggregated	2		2		2		2	
mass pre-dissolution (mg)	1999.4		1654.9		1496.2		1563	
Component Classification	**Grains Counted**	**Counts/Gram**	**Grains Counted**	**Counts/Gram**	**Grains Counted**	**Counts/Gram**	**Grains Counted**	**Counts/Gram**
White glass/mineral	201	100.53	214	129.31	214	143.03	213	136.28
Black (dark) glass/mineral	33	16.50	24	14.50	35	23.39	17	10.88
Vesicular pumice	209	104.53	206	124.48	204	136.35	220	140.75
Non-vesicular lava clast	20	10.00	23	13.90	14	9.36	21	13.44
Altered lava clast	26	13.00	22	13.29	23	15.37	17	10.88
Scoria	11	5.50	10	6.04	11	7.35	12	7.68
TOTAL	500		500		500		500	
Core	U1396C-1H-4W		U1396C-1H-4W		U1396C-1H-4W		U1396C-1H-4W	
Segment of interest (cm downcore)	11-15cm		11-15cm		11-15cm		11-15cm	
Subsection sampled (cm downcore)	13-13.5cm		13.5-14cm		14-14.5cm		14.5-15cm	
cm^3 of material disaggregated	2		2		2		2	
mass pre-dissolution (mg)	1355		1499.8		1898.5		1693.9	
Component Classification	**Grains Counted**	**Counts/Gram**	**Grains Counted**	**Counts/Gram**	**Grains Counted**	**Counts/Gram**	**Grains Counted**	**Counts/Gram**
White glass/mineral	240	177.12	231	154.02	218	114.83	206	121.61
Black (dark) glass/mineral	17	12.55	19	12.67	36	18.96	23	13.58
Vesicular pumice	209	154.24	223	148.69	198	104.29	217	128.11
Non-vesicular lava clast	11	8.12	13	8.67	16	8.43	24	14.17
Altered lava clast	11	8.12	7	4.67	23	12.11	25	14.76
Scoria	12	8.86	7	4.67	9	4.74	5	2.95
TOTAL	500		500	333.38	500		500	

Table 2 Component analysis for core segment 41-45cm

Core	U1396C-1H-4W		U1396C-1H-4W		U1396C-1H-4W		U1396C-1H-4W	
Segment of interest (cm downcore)	41-45cm		41-45cm		41-45cm		41-45cm	
Subsection sampled (cm downcore)	41-41.5cm		41.5-42cm		42-42.5cm		42.5-43cm	
cm^3 of material disaggregated	2		2		2		2	
mass pre-dissolution (mg)	1537.1		2020.3		1479.2		1468.1	
Component Classification	**Grains Counted**	**Counts/Gram**	**Grains Counted**	**Counts/Gram**	**Grains Counted**	**Counts/Gram**	**Grains Counted**	**Counts/Gram**
White glass/mineral	269	175.00	281	139.09	246	166.31	251	170.97
Black (dark) glass/mineral	23	14.96	26	12.87	41	27.72	35	23.84
Vesicular pumice	73	47.49	94	46.53	108	73.01	108	73.56
Non-vesicular lava clast	47	30.58	32	15.84	42	28.39	31	21.12
Altered lava clast	26	16.91	57	28.21	49	33.13	54	36.78
Scoria	15	9.76	10	4.95	14	9.46	21	14.30
TOTAL	500		500		500		500	
Core	U1396C-1H-4W		U1396C-1H-4W		U1396C-1H-4W		U1396C-1H-4W	
Segment of interest (cm downcore)	41-45cm		41-45cm		41-45cm		41-45cm	
Subsection sampled (cm downcore)	43-43.5cm		43.5-44cm		44-44.5cm		44.5-45cm	
cm^3 of material disaggregated	2		2		2		2	
mass pre-dissolution (mg)	1369		1619.9		1842.8		1372.4	
Component Classification	**Grains Counted**	**Counts/Gram**	**Grains Counted**	**Counts/Gram**	**Grains Counted**	**Counts/Gram**	**Grains Counted**	**Counts/Gram**
White glass/mineral	211	154.13	223	137.66	238	129.15	222	161.76
Black (dark) glass/mineral	43	31.41	51	31.48	39	21.16	45	32.79
Vesicular pumice	150	109.57	164	101.24	147	79.77	171	124.60
Non-vesicular lava clast	38	27.76	23	14.20	41	22.25	34	24.77
Altered lava clast	45	32.87	35	21.61	27	14.65	19	13.84
Scoria	13	9.50	4	2.47	8	4.34	9	6.56
TOTAL	500		500		500		500	

8.2 Appendix B: Major & Minor Element Data (EMPA)

Table 1 Cryptotephra glass major element composition as determined by EMPA for interval 11-11.5cm

Particle Number	SiO_2[a]	TiO_2	Al_2O_3	FeO	MnO	MgO	CaO	Na_2O	K_2O	P_2O_5	SO_3	Cr_2O_3	NiO	Total[b]	Mg#
11-11.5_1	69.91	0.44	13.46	2.07	0.00	0.69	2.21	2.93	0.66	0.10	0.01	0.00	0.02	92.50	37.10
11-11.5_6	69.53	0.88	15.30	4.20	0.01	1.06	0.40	0.44	0.25	0.09	0.04	0.01	0.02	92.22	31.03
11-11.5_8	66.21	0.28	18.69	0.65	0.00	0.08	6.91	4.16	0.13	0.05	0.00	0.01	0.03	97.20	17.82
11-11.5_12	72.72	0.15	11.91	1.79	0.07	0.10	1.73	4.01	1.67	0.02	0.05	0.00	0.00	94.23	9.36
11-11.5_13	72.3	0.15	11.88	1.80	0.04	0.13	1.72	4.10	1.69	0.01	0.02	0.00	0.00	93.84	11.25
11-11.5_26	77.65	0.17	11.91	1.26	0.06	0.27	2.11	3.72	1.31	0.00	0.00	0.00	0.00	98.45	27.53
11-11.5_27	73.37	0.16	12.42	1.03	0.02	0.11	1.47	3.35	2.87	0.00	0.00	0.00	0.00	94.80	15.33
11-11.5_33	73.58	0.10	12.20	1.62	0.04	0.10	1.70	4.30	1.69	0.00	0.03	0.00	0.00	95.37	10.16
11-11.5_35	73.86	0.09	12.11	1.72	0.06	0.13	1.65	4.08	1.95	0.00	0.00	0.00	0.00	95.65	12.00
11-11.5_36	73.84	0.10	12.19	1.80	0.08	0.14	1.64	4.20	1.90	0.00	0.00	0.00	0.00	95.89	12.35
11-11.5_38	73.82	0.06	12.13	1.29	0.04	0.04	1.50	4.19	1.78	0.00	0.00	0.00	0.00	94.85	4.84

[a] Oxides reported are NOT normalized to 100% anhydrous values

[b] Totals are the raw unnormalized values obtained from EMPA

Table 2 Cryptotephra glass major element composition as determined by EMPA for Interval 11.5-12cm

Particle Number	SiO_2	TiO_2	Al_2O_3	FeO	MnO	MgO	CaO	Na_2O	K_2O	P_2O_5	SO_3	Cr_2O_3	NiO	Total	Mg#
11.5-12_4	73.24	0.28	13.09	1.76	0.07	0.53	2.62	3.82	1.61	0.08	0.02	0.00	0.00	97.12	34.93
11.5-12_5	68.40	0.21	17.10	1.12	0.03	0.39	5.00	4.21	1.18	0.02	0.00	0.03	0.00	97.68	38.31
11.5-12_8	73.52	0.13	12.03	1.55	0.03	0.11	1.56	4.15	1.73	0.00	0.00	0.02	0.00	94.82	11.23
11.5-12_11	74.42	0.11	12.13	1.50	0.04	0.12	1.66	4.38	1.85	0.01	0.01	0.01	0.04	96.29	12.13
11.5-12_16	66.78	0.96	11.69	7.64	0.16	0.47	2.63	4.35	1.22	0.34	0.04	0.03	0.05	96.36	9.85
11.5-12_17	67.28	0.19	14.86	3.02	0.12	0.46	4.22	4.43	1.07	0.10	0.00	0.03	0.05	95.83	21.49
11.5-12_27	67.45	0.41	14.17	3.07	0.07	0.26	3.27	4.49	1.47	0.15	0.00	0.00	0.00	94.81	13.22
11.5-12_38	78.68	0.26	11.67	0.85	0.05	0.33	3.13	3.39	0.21	0.05	0.00	0.00	0.00	98.62	40.73
11.5-12_39	71.58	0.20	10.86	0.62	0.04	0.08	2.85	3.90	0.21	0.05	0.01	0.00	0.00	90.40	18.19

Table 3 Cryptotephra glass major element composition as determined by EMPA for Interval 12-12.5cm

Particle Number	SiO_2	TiO_2	Al_2O_3	FeO	MnO	MgO	CaO	Na_2O	K_2O	P_2O_5	SO_3	Cr_2O_3	NiO	Total	Mg#
12-12.5_1	74.39	0.12	11.51	1.68	0.06	0.12	1.41	4.32	1.91	0.00	0.00	0.00	0.00	95.52	11.13
12-12.5_2	76.12	0.92	10.13	1.98	0.06	0.03	0.72	3.03	5.24	0.04	0.00	0.00	0.00	98.26	2.59
12-12.5_22	66.32	0.60	17.36	2.50	0.08	0.73	5.48	4.96	0.45	0.14	0.07	0.00	0.00	98.70	34.18
12-12.5_30	79.68	0.15	11.48	0.72	0.03	0.30	2.52	3.88	0.32	0.02	0.00	0.00	0.00	99.08	42.71
12-12.5_33	73.01	0.24	11.15	2.58	0.16	1.25	2.11	3.47	1.61	0.05	0.00	0.01	0.00	95.64	46.32
12-12.5_34	67.75	0.17	17.64	1.23	0.06	0.30	5.54	4.29	0.89	0.04	0.00	0.00	0.01	97.92	30.65
12-12.5_35	68.04	0.14	17.81	0.85	0.05	0.07	5.25	4.75	1.07	0.06	0.00	0.00	0.00	98.09	12.40
12-12.5_40	65.13	0.57	15.60	4.66	0.15	0.69	4.85	4.33	0.91	0.20	0.01	0.01	0.00	97.10	20.81

Table 4 Cryptotephra glass major element composition as determined by EMPA for Interval 12.5-13cm

Particle Number	SiO_2	TiO_2	Al_2O_3	FeO	MnO	MgO	CaO	Na_2O	K_2O	P_2O_5	SO_3	Cr_2O_3	NiO	Total	Mg#
12.5-13_1	83.70	0.17	9.53	0.26	0.02	0.02	2.51	2.99	0.34	0.02	0.01	0.02	0.00	99.59	10.64
12.5-13_2	80.79	0.12	9.44	1.54	0.09	1.19	2.47	3.07	0.33	0.01	0.01	0.00	0.01	99.08	57.95
12.5-13_4	77.55	0.10	11.48	0.26	0.00	0.06	1.78	3.55	2.44	0.00	0.00	0.00	0.03	97.25	29.98
12.5-13_5	74.07	0.12	11.89	1.49	0.07	0.09	1.46	4.34	2.12	0.00	0.01	0.00	0.00	95.65	9.40
12.5-13_6	73.90	0.11	11.65	1.42	0.07	0.08	1.27	4.00	2.23	0.00	0.00	0.00	0.01	94.73	8.71
12.5-13_7	74.39	0.10	11.69	1.28	0.05	0.07	1.35	4.07	2.06	0.00	0.03	0.00	0.01	95.10	8.71
12.5-13_9	72.36	0.26	12.54	1.98	0.05	0.37	2.62	3.84	1.35	0.01	0.00	0.00	0.01	95.38	24.99
12.5-13_10	76.58	0.09	13.93	0.25	0.00	0.02	4.20	3.88	0.45	0.00	0.01	0.00	0.01	99.44	14.52
12.5-13_16	84.72	0.06	8.98	0.27	0.03	0.07	1.53	3.57	0.32	0.01	0.01	0.02	0.03	99.63	31.96
12.5-13_21	71.19	0.12	16.37	1.14	0.03	0.31	5.42	4.24	0.71	0.02	0.03	0.02	0.00	99.59	32.97
12.5-13_22	66.93	0.30	19.42	0.89	0.05	0.05	6.19	5.12	0.73	0.04	0.01	0.01	0.00	99.73	8.67
12.5-13_23	66.23	0.12	13.10	1.75	0.06	0.07	2.92	3.36	2.12	0.08	0.05	0.00	0.00	89.85	6.74
12.5-13_24	76.24	0.16	13.73	1.20	0.05	0.41	4.96	3.56	0.26	0.00	0.00	0.00	0.00	100.57	37.84
12.5-13_26	90.28	0.14	4.56	0.29	0.00	0.03	1.37	1.27	0.23	0.01	0.01	0.00	0.00	98.19	17.75
12.5-13_35	72.40	0.02	16.85	0.28	0.00	0.00	5.31	4.58	0.23	0.02	0.00	0.00	0.00	99.69	0.00
12.5-13_37	73.18	0.11	12.07	1.67	0.00	0.12	1.59	4.08	1.82	0.01	0.02	0.00	0.00	94.66	11.19

Table 5 Cryptotephra glass major element composition as determined by EMPA for Interval 13.5-14cm

Particle Number	SiO_2	TiO_2	Al_2O_3	FeO	MnO	MgO	CaO	Na_2O	K_2O	P_2O_5	SO_3	Cr_2O_3	NiO	Total	Mg#
13.5-14_1	73.29	0.08	14.27	0.43	0.03	0.06	2.70	4.12	2.44	0.03	0.02	0.00	0.00	97.48	19.86
13.5-14_2	70.97	0.18	12.63	1.66	0.12	0.42	2.24	3.30	3.08	0.06	0.00	0.00	0.00	94.66	31.09
13.5-14_3	69.91	0.31	13.09	1.97	0.11	0.61	2.92	3.71	1.89	0.07	0.00	0.00	0.00	94.59	35.42
13.5-14_5	67.43	0.44	15.87	1.89	0.09	0.23	3.91	3.99	2.59	0.11	0.00	0.00	0.00	96.56	17.78
13.5-14_8	76.86	0.13	12.47	0.56	0.07	0.23	3.42	3.78	0.30	0.04	0.00	0.00	0.00	97.87	42.60
13.5-14_9	73.06	0.15	12.25	2.83	0.22	1.47	3.76	3.79	0.30	0.02	0.01	0.00	0.00	97.86	48.10
13.5-14_10	78.68	0.09	11.62	0.29	0.03	0.01	3.23	3.75	0.25	0.02	0.00	0.00	0.00	97.95	5.53
13.5-14_12	63.52	0.09	19.02	0.45	0.01	0.00	4.20	6.33	1.15	0.00	0.05	0.00	0.00	94.82	0.00
13.5-14_13	78.42	0.09	12.32	0.66	0.03	0.30	3.02	3.89	0.36	0.01	0.01	0.00	0.00	99.10	44.45
13.5-14_17	75.40	0.06	12.71	1.57	0.00	0.03	1.29	4.97	2.28	0.13	0.04	0.00	0.00	98.49	3.27
13.5-14_18	74.91	0.13	12.67	1.13	0.04	0.22	2.39	3.53	2.00	0.00	0.03	0.00	0.00	97.05	25.44
13.5-14_20	74.43	0.14	12.37	1.22	0.05	0.21	1.78	3.44	2.71	0.01	0.01	0.00	0.00	96.38	23.67
13.5-14_21	77.49	0.10	12.44	0.89	0.02	0.01	1.57	5.23	1.13	0.04	0.00	0.02	0.02	98.96	1.80
13.5-14_22	73.12	0.15	11.99	1.51	0.07	0.09	1.55	4.21	1.88	0.01	0.00	0.03	0.00	94.63	10.00
13.5-14_23	73.34	0.15	11.80	1.62	0.10	0.13	1.56	4.27	1.93	0.01	0.00	0.04	0.00	94.95	12.67
13.5-14_24	72.96	0.16	11.59	2.14	0.10	0.24	1.64	4.14	1.88	0.01	0.00	0.02	0.02	94.90	16.91
13.5-14_25	87.30	0.04	7.41	0.13	0.03	0.00	1.90	2.28	0.25	0.01	0.02	0.08	0.02	99.47	0.00
13.5-14_26	72.35	0.38	12.02	2.23	0.10	0.33	1.88	3.37	3.12	0.07	0.00	0.05	0.03	95.93	20.62
13.5-14_27	79.19	0.26	10.94	0.71	0.05	0.18	2.23	3.99	0.51	0.05	0.02	0.06	0.02	98.21	30.95
13.5-14_30	73.89	0.35	14.01	1.89	0.07	0.23	3.79	4.50	0.27	0.09	0.00	0.05	0.04	99.19	18.00
13.5-14_33	73.97	0.12	11.80	1.41	0.07	0.06	1.16	2.66	4.53	0.00	0.00	0.00	0.00	95.77	6.53
13.5-14_34	73.67	0.13	11.91	1.64	0.07	0.09	1.55	4.13	1.96	0.01	0.00	0.00	0.00	95.16	9.14
13.5-14_35	67.46	0.12	10.69	1.52	0.04	0.11	1.48	4.03	1.77	0.02	0.15	0.00	0.00	87.39	11.44
13.5-14_38	74.44	0.53	12.57	2.47	0.06	0.46	3.22	4.28	0.54	0.08	0.01	0.00	0.00	98.67	25.08
13.5-14_40	79.15	0.12	11.48	1.17	0.08	0.32	2.44	3.96	0.57	0.02	0.00	0.00	0.00	99.31	33.08

Table 6 Cryptotephra glass major element composition as determined by EMPA for Interval 14-14.5cm

Particle Number	SiO_2	TiO_2	Al_2O_3	FeO	MnO	MgO	CaO	Na_2O	K_2O	P_2O_5	SO_3	Cr_2O_3	NiO	Total	Mg#
14-14.5_1	72.35	0.41	11.47	2.58	0.12	0.75	1.60	3.21	3.60	0.12	0.00	0.00	0.00	96.20	34.09
14-14.5_2	71.84	0.43	12.36	2.86	0.11	0.79	2.11	3.66	3.22	0.09	0.00	0.00	0.00	97.47	32.98
14-14.5_19	69.65	0.02	17.02	0.37	0.01	0.01	4.05	5.73	0.32	0.00	0.00	0.00	0.00	97.18	4.41
14-14.5_33	74.08	0.15	12.11	1.94	0.06	0.20	1.70	4.22	1.82	0.01	0.00	0.00	0.01	96.30	15.60

Table 7 Cryptotephra glass major element composition as determined by EMPA for Interval 14.5-15cm

Particle Number	SiO_2	TiO_2	Al_2O_3	FeO	MnO	MgO	CaO	Na_2O	K_2O	P_2O_5	SO_3	Cr_2O_3	NiO	Total	Mg#
14.5-15_1	70.88	0.52	12.79	2.51	0.10	0.59	2.44	4.12	2.32	0.12	0.01	0.02	0.02	96.43	29.40
14.5-15_2	58.31	1.17	15.94	6.53	0.16	2.29	5.71	3.84	0.28	0.08	0.04	0.04	0.03	94.41	38.47
14.5-15_4	59.21	0.97	15.39	9.36	0.22	2.25	6.52	4.04	0.42	0.32	0.01	0.01	0.00	98.71	30.00
14.5-15_5	66.48	0.12	16.68	3.66	0.13	0.61	4.96	4.84	0.87	0.11	0.02	0.00	0.00	98.48	22.97
14.5-15_6	73.35	0.09	12.71	1.35	0.01	0.04	1.77	4.49	1.81	0.00	0.00	0.00	0.00	95.62	4.90
14.5-15_10	73.58	0.08	11.79	1.45	0.01	0.05	1.51	4.06	1.88	0.02	0.00	0.00	0.00	94.43	6.24
14.5-15_11	74.33	0.10	11.86	1.39	0.02	0.04	1.49	4.13	2.05	0.00	0.00	0.00	0.00	95.40	4.80
14.5-15_12	74.17	0.08	11.91	1.36	0.03	0.04	1.41	4.10	2.24	0.01	0.00	0.00	0.00	95.35	4.93
14.5-15_13	73.70	0.11	11.95	1.65	0.03	0.13	1.69	4.22	2.10	0.01	0.00	0.00	0.00	95.59	12.01
14.5-15_14	74.23	0.13	12.46	1.65	0.10	0.13	1.64	4.31	2.06	0.02	0.03	0.04	0.00	96.78	12.00
14.5-15_17	73.69	0.15	12.25	1.47	0.07	0.08	1.39	4.22	2.27	0.01	0.00	0.04	0.00	95.64	8.40
14.5-15_18	73.77	0.11	12.61	1.65	0.06	0.08	1.90	4.44	1.81	0.03	0.02	0.03	0.00	96.53	8.25
14.5-15_21	70.82	0.20	16.10	1.70	0.07	0.63	4.84	4.31	0.21	0.03	0.03	0.01	0.00	98.94	39.86
14.5-15_24	74.67	0.20	13.94	1.60	0.09	0.51	3.04	4.04	1.55	0.08	0.01	0.00	0.00	99.73	36.12
14.5-15_25	75.73	0.23	12.47	1.30	0.08	0.21	2.36	3.76	1.78	0.05	0.02	0.00	0.00	97.99	22.41
14.5-15_26	74.86	0.12	12.38	1.59	0.06	0.11	1.73	4.40	1.90	0.01	0.00	0.03	0.00	97.19	11.16
14.5-15_27	74.13	0.31	12.19	2.97	0.11	0.79	2.71	4.01	1.55	0.06	0.02	0.02	0.00	98.87	32.22
14.5-15_31	69.24	0.40	14.26	2.72	0.11	0.81	2.96	4.20	2.58	0.09	0.01	0.02	0.00	97.40	34.61
14.5-15_32	77.42	0.36	11.39	2.55	0.13	0.82	2.68	3.88	0.79	0.14	0.00	0.02	0.01	100.21	36.32
14.5-15_35	74.87	0.15	12.29	1.46	0.08	0.15	1.44	4.03	2.18	0.01	0.01	0.05	0.03	96.74	15.84

Table 8 Cryptotephra glass major element composition as determined by EMPA for Interval 41-41.5cm

Particle Number	SiO_2	TiO_2	Al_2O_3	FeO	MnO	MgO	CaO	Na_2O	K_2O	P_2O_5	SO_3	Cr_2O_3	NiO	Total	Mg#
41-41.5_2	76.89	0.09	12.14	1.67	0.05	0.09	1.47	0.69	1.74	0.00	0.00	0.00	0.00	94.83	8.45
41-41.5_3	74.96	0.09	11.91	2.00	0.04	0.14	1.59	4.17	1.83	0.03	0.00	0.00	0.00	96.76	11.37
41-41.5_4	75.24	0.09	11.99	1.51	0.02	0.07	1.50	4.27	1.81	0.00	0.00	0.00	0.00	96.50	7.73
41-41.5_5	74.77	0.10	11.67	2.14	0.05	0.17	1.63	4.01	1.84	0.00	0.01	0.00	0.00	96.39	12.62
41-41.5_6	74.57	0.11	11.87	1.98	0.05	0.16	1.65	4.19	1.76	0.01	0.00	0.00	0.00	96.35	12.70
41-41.5_8	81.95	0.07	10.99	0.58	0.00	0.28	2.78	3.51	0.43	0.03	0.04	0.00	0.00	100.66	46.03
41-41.5_10	78.48	0.03	11.69	1.48	0.02	0.23	1.67	2.67	4.01	0.06	0.01	0.00	0.00	100.36	21.71
41-41.5_13	79.79	0.08	12.80	0.26	0.00	0.01	3.35	3.99	0.57	0.01	0.00	0.00	0.00	100.87	6.86
41-41.5_16	74.94	0.16	11.93	1.77	0.06	0.12	1.70	4.27	1.84	0.01	0.00	0.00	0.01	96.83	10.94
41-41.5_17	74.84	0.18	11.95	1.77	0.07	0.14	1.68	4.43	1.81	0.06	0.00	0.00	0.01	96.93	12.26
41-41.5_19	77.71	0.17	12.51	1.50	0.07	0.08	1.56	4.39	1.91	0.01	0.00	0.00	0.00	99.90	8.82
41-41.5_20	77.53	0.18	12.51	1.69	0.06	0.14	1.71	4.43	1.92	0.04	0.00	0.00	0.00	100.22	13.09
41-41.5_21	76.24	0.13	11.45	1.50	0.05	0.08	1.29	4.10	2.14	0.03	0.00	0.00	0.00	97.00	8.18
41-41.5_22	74.20	0.16	11.97	1.74	0.06	0.14	1.53	3.62	2.39	0.02	0.00	0.00	0.00	95.83	12.28
41-41.5_24	75.81	0.11	12.14	1.76	0.04	0.13	1.64	3.14	1.90	0.02	0.00	0.03	0.00	96.71	11.25
41-41.5_25	74.83	0.11	12.13	1.78	0.04	0.15	1.69	4.22	1.85	0.01	0.00	0.01	0.00	96.81	12.78
41-41.5_26	82.80	0.06	11.04	0.21	0.00	0.01	3.09	3.21	0.14	0.02	0.00	0.02	0.00	100.59	5.33
41-41.5_27	75.05	0.08	11.64	1.63	0.03	0.09	1.37	4.21	1.77	0.05	0.00	0.01	0.00	95.93	9.00
41-41.5_29	75.05	0.09	12.08	1.73	0.04	0.19	1.76	4.35	1.84	0.05	0.00	0.00	0.00	97.18	16.36
41-41.5_30	82.53	0.20	10.08	0.33	0.00	0.03	2.76	2.89	0.26	0.03	0.01	0.00	0.00	99.13	15.72
41-41.5_32	74.62	0.16	12.75	1.65	0.05	0.42	2.48	3.84	1.55	0.03	0.01	0.01	0.00	97.57	31.16
41-41.5_33	75.39	0.18	13.31	1.26	0.06	0.20	2.66	4.19	1.44	0.04	0.00	0.00	0.00	98.73	21.78
41-41.5_34	77.36	0.15	12.59	1.87	0.06	0.16	1.70	4.31	1.91	0.02	0.00	0.00	0.00	100.13	13.12
41-41.5_36	73.66	0.12	11.84	1.82	0.05	0.14	1.58	4.05	1.73	0.03	0.00	0.00	0.00	95.02	12.16

Table 9 Cryptotephra glass major element composition as determined by EMPA for Interval 41.5-42cm

Particle Number	SiO_2	TiO_2	Al_2O_3	FeO	MnO	MgO	CaO	Na_2O	K_2O	P_2O_5	SO_3	Cr_2O_3	NiO	Total	Mg#
41.5-42_1	74.02	0.14	12.00	1.60	0.06	0.08	1.59	4.41	1.79	0.01	0.02	0.00	0.00	95.72	8.64
41.5-42_2	72.83	0.17	12.31	1.64	0.08	0.12	1.84	4.27	1.78	0.00	0.02	0.00	0.00	95.06	11.90
41.5-42_3	72.11	0.14	11.70	2.30	0.11	0.31	2.01	4.14	1.70	0.01	0.02	0.00	0.00	94.55	19.27
41.5-42_4	72.65	0.17	11.87	1.50	0.09	0.07	1.56	2.15	1.79	0.00	0.01	0.00	0.00	91.85	7.39
41.5-42_5	72.32	0.23	11.99	0.75	0.06	0.05	1.87	4.03	2.18	0.05	0.00	0.00	0.00	93.54	11.31
41.5-42_6	78.16	0.20	12.44	0.76	0.04	0.04	1.94	3.57	2.30	0.04	0.00	0.00	0.01	99.49	8.62
41.5-42_7	78.85	0.23	12.16	1.33	0.08	0.30	2.33	3.95	1.35	0.04	0.00	0.02	0.00	100.64	28.71
41.5-42_8	74.42	0.14	12.17	1.64	0.06	0.12	1.75	4.26	1.85	0.01	0.00	0.00	0.00	96.41	11.53
41.5-42_9	75.24	0.11	11.94	1.49	0.05	0.07	1.46	4.25	1.92	0.00	0.02	0.00	0.00	96.56	7.99
41.5-42_10	74.72	0.14	12.13	1.73	0.08	0.13	1.74	4.21	1.82	0.01	0.03	0.00	0.00	96.74	11.90
41.5-42_11	74.74	0.12	11.86	1.74	0.08	0.09	1.65	4.12	1.82	0.02	0.00	0.00	0.00	96.24	8.80
41.5-42_12	74.23	0.13	11.98	1.90	0.10	0.17	1.66	4.09	1.84	0.00	0.00	0.00	0.00	96.10	13.73
41.5-42_13	75.29	0.14	11.77	1.76	0.07	0.08	1.52	4.11	1.96	0.01	0.01	0.01	0.00	96.72	7.65
41.5-42_14	75.45	0.11	11.97	1.79	0.07	0.11	1.52	4.31	1.96	0.02	0.01	0.00	0.00	97.32	9.76
41.5-42_15	73.14	0.11	11.56	1.74	0.06	0.10	1.41	3.72	3.00	0.00	0.01	0.00	0.00	94.85	9.19
41.5-42_16	74.26	0.15	11.80	1.96	0.08	0.19	1.52	3.83	2.90	0.00	0.00	0.01	0.01	96.72	14.85
41.5-42_17	73.67	0.13	12.11	1.83	0.07	0.13	1.59	4.24	2.17	0.00	0.00	0.01	0.01	95.96	11.35
41.5-42_18	74.17	0.15	11.54	2.53	0.11	0.30	1.78	3.90	2.21	0.01	0.00	0.01	0.00	96.71	17.57
41.5-42_19	74.78	0.18	11.68	2.44	0.11	0.29	1.78	2.03	2.16	0.00	0.00	0.02	0.00	95.46	17.31
41.5-42_20	74.02	0.13	12.16	1.81	0.04	0.14	1.67	4.18	1.92	0.03	0.00	0.00	0.00	96.10	11.95
41.5-42_21	74.46	0.14	12.22	1.89	0.09	0.15	1.66	4.23	1.91	0.01	0.00	0.01	0.00	96.76	12.31
41.5-42_22	74.44	0.16	11.84	1.78	0.07	0.12	1.59	4.33	1.94	0.02	0.00	0.02	0.01	96.32	10.57
41.5-42_24	75.35	0.14	12.03	1.65	0.07	0.12	1.66	4.24	1.99	0.00	0.01	0.00	0.00	97.26	11.19
41.5-42_25	75.75	0.13	12.00	1.65	0.06	0.06	1.54	4.41	1.99	0.00	0.00	0.00	0.00	97.59	5.78
41.5-42_26	77.11	0.23	11.64	1.69	0.10	0.32	1.72	3.59	1.89	0.09	0.01	0.00	0.00	98.38	25.08
41.5-42_27	76.92	0.14	12.33	1.85	0.07	0.13	1.68	4.44	1.99	0.03	0.00	0.00	0.01	99.59	11.11
41.5-42_28	75.55	0.14	11.82	1.71	0.06	0.14	1.52	4.29	1.93	0.02	0.00	0.00	0.00	97.17	12.43
41.5-42_29	77.06	0.21	11.97	1.17	0.07	0.16	1.85	3.66	1.93	0.03	0.04	0.00	0.00	98.15	19.44
41.5-42_30	73.57	0.16	12.41	2.61	0.12	0.34	1.73	4.31	2.68	0.02	0.00	0.00	0.00	97.95	19.03
41.5-42_31	77.18	0.15	12.70	1.07	0.04	0.05	2.16	4.72	1.32	0.03	0.03	0.00	0.00	99.44	7.84
41.5-42_32	77.72	0.15	12.26	1.19	0.04	0.08	1.96	4.56	1.54	0.06	0.00	0.00	0.01	99.56	10.67

41.5-42_33	74.92	0.14	12.22	1.55	0.05	0.08	1.67	4.47	1.76	0.01	0.04	0.00	0.00	96.91	8.23
41.5-42_34	73.85	0.14	11.79	1.81	0.06	0.15	1.60	4.14	1.82	0.02	0.04	0.00	0.00	95.43	12.84

Table 10 Cryptotephra glass major element composition as determined by EMPA for Interval 42-42.5cm

Particle Number	SiO_2	TiO_2	Al_2O_3	FeO	MnO	MgO	CaO	Na_2O	K_2O	P_2O_5	SO_3	Cr_2O_3	NiO	Total	Mg#
42-42.5_1	75.31	0.13	12.32	1.85	0.08	0.10	1.60	4.21	1.80	0.02	0.00	0.00	0.00	97.42	9.16
42-42.5_2	75.23	0.12	12.17	1.49	0.08	0.08	1.33	4.47	1.99	0.01	0.00	0.02	0.00	97.00	9.01
42-42.5_3	75.63	0.10	12.58	1.39	0.06	0.11	1.86	4.54	1.51	0.02	0.00	0.01	0.00	97.81	12.57
42-42.5_5	73.93	0.12	12.03	1.78	0.10	0.14	1.67	4.17	1.83	0.01	0.00	0.00	0.00	95.78	11.94
42-42.5_7	72.82	0.10	11.76	1.64	0.07	0.10	1.42	4.20	2.10	0.03	0.00	0.00	0.02	94.26	9.79
42-42.5_8	75.64	0.12	12.36	1.64	0.07	0.10	1.59	4.22	2.14	0.00	0.00	0.00	0.00	97.88	9.55
42-42.5_9	76.40	0.10	12.69	1.79	0.08	0.11	1.78	3.93	1.95	0.01	0.00	0.02	0.00	98.87	9.98
42-42.5_11	73.54	0.22	12.11	4.88	0.06	0.09	1.53	4.14	1.88	0.01	0.02	0.01	0.00	98.50	3.34
42-42.5_12	74.29	0.08	11.97	1.33	0.06	0.09	1.45	4.30	1.98	0.03	0.00	0.00	0.00	95.58	10.45
42-42.5_13	75.14	0.28	12.93	1.80	0.08	0.28	2.51	3.52	1.86	0.08	0.00	0.02	0.00	98.50	21.96
42-42.5_14	73.63	0.26	13.12	1.84	0.10	0.44	2.79	3.79	1.59	0.09	0.01	0.00	0.00	97.65	29.67
42-42.5_15	74.37	0.27	13.33	1.90	0.10	0.43	2.82	2.49	1.60	0.04	0.00	0.01	0.00	97.36	28.87
42-42.5_18	73.85	0.19	12.23	2.02	0.12	0.58	2.07	3.41	2.35	0.14	0.01	0.00	0.00	96.98	33.97
42-42.5_17	73.41	0.21	12.29	1.60	0.09	0.31	1.68	3.50	2.75	0.03	0.00	0.01	0.00	95.89	25.84
42-42.5_18	74.88	0.20	12.56	1.35	0.07	0.25	2.02	3.42	2.15	0.05	0.02	0.02	0.00	96.99	24.93
42-42.5_19	74.91	0.23	12.44	1.74	0.12	0.43	2.25	3.63	1.86	0.05	0.02	0.00	0.00	97.68	30.70
42-42.5_24	74.79	0.11	12.29	1.35	0.03	0.05	1.51	4.38	1.97	0.02	0.00	0.00	0.00	96.50	6.27
42-42.5_25	74.99	0.12	12.37	2.22	0.08	0.26	1.89	4.37	1.96	0.00	0.00	0.00	0.00	98.27	17.02
42-42.5_27	74.58	0.12	12.20	1.83	0.04	0.11	1.59	4.25	1.95	0.00	0.00	0.00	0.00	96.67	9.71
42-42.5_26	74.39	0.10	12.17	1.49	0.02	0.09	1.55	4.11	1.93	0.01	0.00	0.00	0.00	95.86	9.31
42-42.5_29	69.78	0.20	15.03	0.91	0.01	0.08	3.68	3.48	2.38	0.05	0.00	0.00	0.00	95.59	12.90
42-42.5_30	73.84	0.35	11.55	4.00	0.11	0.60	2.00	2.76	2.93	0.09	0.02	0.00	0.01	98.26	20.99
42-42.5_32	73.63	0.22	13.00	1.83	0.06	0.63	2.78	2.89	2.76	0.05	0.02	0.00	0.00	97.86	37.88
42-42.5_33	74.80	0.10	12.19	1.62	0.05	0.12	1.66	4.57	1.92	0.01	0.00	0.00	0.00	97.04	11.40
42-42.5_34	76.91	0.10	12.28	1.42	0.03	0.09	1.52	4.43	1.93	0.01	0.00	0.00	0.01	98.74	10.18
42-42.5_35	75.00	0.08	13.81	1.31	0.04	0.07	2.07	4.90	1.78	0.00	0.01	0.01	0.00	99.08	8.23
42-42.5_36	75.93	0.10	12.91	1.65	0.05	0.15	1.91	4.66	1.84	0.00	0.00	0.00	0.00	99.20	13.86
42-42.5_37	74.45	0.08	11.90	2.08	0.06	0.26	1.80	4.03	1.85	0.01	0.01	0.00	0.00	96.55	18.41
42-42.5_38	76.31	0.12	12.57	1.66	0.07	0.11	1.59	4.43	1.99	0.01	0.00	0.00	0.00	98.84	10.15
42-42.5_39	76.04	0.12	12.71	1.70	0.03	0.12	1.62	4.58	1.96	0.01	0.02	0.00	0.00	98.89	10.94
42-42.5_40	75.54	0.12	12.34	1.57	0.07	0.11	1.63	4.12	1.79	0.03	0.03	0.00	0.00	97.36	11.42

Table 11 Cryptotephra glass major element composition as determined by EMPA for Interval 43-43.5cm

Particle Number	SiO_2	TiO_2	Al_2O_3	FeO	MnO	MgO	CaO	Na_2O	K_2O	P_2O_5	SO_3	Cr_2O_3	NiO	Total	Mg#
43-43.5_2	74.07	0.15	12.55	1.58	0.04	0.08	1.68	4.33	1.72	0.00	0.00	0.00	0.00	96.20	8.41
43-43.5_3	73.92	0.15	12.20	1.49	0.05	0.07	1.55	4.18	1.81	0.02	0.00	0.00	0.00	95.44	8.03
43-43.5_5	75.54	0.28	12.27	1.70	0.08	0.32	2.25	3.76	1.60	0.04	0.00	0.00	0.00	97.84	25.31
43-43.5_7	73.37	0.16	11.92	1.64	0.07	0.12	1.53	4.17	1.76	0.03	0.00	0.00	0.00	94.77	11.73
43-43.5_8	74.21	0.18	12.15	1.66	0.06	0.12	1.55	1.12	1.75	0.03	0.00	0.00	0.00	92.82	11.04
43-43.5_13	72.58	0.28	13.20	1.74	0.04	0.14	1.76	3.37	3.51	0.07	0.00	0.02	0.00	96.71	12.64
43-43.5_15	73.78	0.07	11.86	1.56	0.07	0.08	1.41	4.06	1.79	0.04	0.00	0.00	0.00	94.72	8.26
43-43.5_16	74.00	0.10	11.73	1.42	0.05	0.05	1.38	4.16	1.77	0.01	0.00	0.00	0.00	94.67	5.41
43-43.5_20	73.53	0.30	13.99	1.83	0.07	0.42	2.93	4.20	1.97	0.06	0.00	0.01	0.00	99.31	28.90
43-43.5_23	74.23	0.08	11.78	1.19	0.04	0.01	0.92	3.79	2.72	0.02	0.03	0.00	0.00	94.81	0.80
43-43.5_24	74.64	0.12	11.70	1.57	0.06	0.07	1.36	4.22	1.86	0.01	0.01	0.00	0.00	95.63	7.72
43-43.5_25	73.39	0.13	12.05	2.53	0.04	0.02	1.55	4.33	1.69	0.05	0.03	0.00	0.00	95.80	1.12
43-43.5_27	79.13	0.44	12.55	0.55	0.02	0.00	3.30	4.16	0.34	0.08	0.00	0.00	0.00	100.57	0.00
43-43.5_28	71.36	0.34	14.25	1.76	0.06	0.11	2.27	4.58	2.81	0.06	0.01	0.01	0.00	97.61	9.77
43-43.5_33	74.90	0.21	12.38	1.21	0.09	0.24	2.26	3.59	1.71	0.06	0.03	0.02	0.00	96.70	26.32
43-43.5_34	74.90	0.23	12.55	1.39	0.11	0.31	2.39	3.71	1.65	0.08	0.00	0.00	0.02	97.33	28.29
43-43.5_35	84.14	0.09	10.02	0.14	0.01	0.03	2.38	3.20	0.41	0.02	0.00	0.03	0.01	100.48	24.64
43-43.5_36	79.65	0.08	12.66	0.12	0.00	0.01	3.20	4.20	0.29	0.04	0.00	0.01	0.00	100.27	14.59
43-43.5_37	75.41	0.14	12.10	1.68	0.07	0.16	1.49	4.47	1.80	0.03	0.00	0.03	0.03	97.41	14.26
43-43.5_38	76.51	0.28	10.59	1.31	0.09	0.21	1.33	2.41	2.88	0.03	0.00	0.01	0.03	95.68	21.82
43-43.5_40	73.32	0.14	12.12	1.65	0.08	0.13	1.55	2.65	1.85	0.02	0.02	0.01	0.02	93.57	12.60

Table 12 Cryptotephra glass major element composition as determined by EMPA for Interval 43.5-44cm

Particle Number	SiO_2	TiO_2	Al_2O_3	FeO	MnO	MgO	CaO	Na_2O	K_2O	P_2O_5	SO_3	Cr_2O_3	NiO	Total	Mg#
43.5-44_1	84.55	0.12	9.86	0.19	0.02	0.01	2.15	3.08	0.81	0.01	0.00	0.02	0.00	100.82	8.48
43.5-44_3	71.34	0.32	13.92	2.13	0.06	0.32	2.60	4.22	2.21	0.03	0.01	0.01	0.00	97.18	21.30
43.5-44_6	76.23	0.14	12.83	1.67	0.06	0.10	1.61	4.25	1.88	0.02	0.00	0.01	0.01	98.81	9.61
43.5-44_7	75.95	0.18	12.79	1.79	0.05	0.12	1.64	4.32	1.91	0.00	0.00	0.00	0.00	98.74	10.71
43.5-44_8	75.83	0.12	12.61	1.86	0.06	0.15	1.68	4.29	1.87	0.02	0.00	0.02	0.00	98.50	12.29
43.5-44_9	76.04	0.13	12.85	1.70	0.07	0.10	1.58	4.45	1.90	0.02	0.00	0.02	0.00	98.86	9.82
43.5-44_10	74.52	0.14	12.46	1.60	0.06	0.07	1.49	4.18	1.86	0.00	0.00	0.03	0.00	96.41	7.62
43.5-44_13	93.70	0.04	4.63	0.13	0.00	0.00	1.20	1.48	0.10	0.00	0.00	0.00	0.00	101.27	0.00
43.5-44_20	77.36	0.09	12.58	1.58	0.05	0.11	1.44	4.58	1.82	0.01	0.00	0.00	0.00	99.63	11.42
43.5-44_21	75.05	0.18	12.24	1.79	0.07	0.08	1.62	4.35	1.87	0.00	0.00	0.00	0.00	97.25	7.79
43.5-44_22	73.79	0.14	12.14	1.96	0.07	0.16	1.71	4.11	1.87	0.03	0.00	0.00	0.00	95.99	12.99
43.5-44_23	74.10	0.17	12.16	1.61	0.07	0.10	1.60	4.20	1.86	0.00	0.00	0.00	0.00	95.87	10.08
43.5-44_24	75.65	0.23	11.90	1.44	0.10	0.24	1.86	3.39	2.33	0.04	0.01	0.00	0.00	97.19	23.06
43.5-44_25	75.54	0.18	12.13	1.51	0.10	0.29	1.99	3.40	2.21	0.04	0.00	0.00	0.00	97.40	25.42
43.5-44_26	75.03	0.15	12.29	1.50	0.05	0.08	1.58	4.38	1.97	0.01	0.00	0.01	0.00	97.04	8.31
43.5-44_27	74.49	0.17	12.15	1.99	0.08	0.20	1.80	4.23	1.93	0.00	0.01	0.01	0.00	97.05	14.94
43.5-44_28	74.46	0.15	12.28	1.66	0.07	0.11	1.67	4.42	1.91	0.00	0.00	0.00	0.00	96.73	10.54
43.5-44_33	74.19	0.12	11.81	1.54	0.06	0.06	1.36	3.85	2.72	0.03	0.01	0.01	0.00	95.78	6.93
43.5-44_34	74.58	0.12	11.93	1.36	0.06	0.05	1.25	3.88	2.73	0.06	0.00	0.00	0.00	96.02	5.88
43.5-44_35	73.63	0.16	11.72	2.32	0.10	0.19	1.73	3.95	2.58	0.02	0.02	0.00	0.00	96.42	12.72
43.5-44_36	73.99	0.12	12.15	1.60	0.05	0.09	1.61	4.19	1.96	0.04	0.00	0.02	0.00	95.81	8.97
43.5-44_37	74.83	0.10	12.35	1.47	0.05	0.07	1.56	4.13	1.92	0.04	0.02	0.02	0.00	96.56	8.06
43.5-44_38	78.72	0.56	11.08	2.40	0.08	0.37	2.45	4.05	0.33	0.14	0.00	0.00	0.00	100.19	21.43
43.5-44_39	74.23	0.53	11.19	5.20	0.20	1.53	2.95	3.84	0.31	0.13	0.01	0.03	0.01	100.18	34.47

Table 13 Cryptotephra glass major element composition as determined by EMPA for Interval 44-44.5cm

Particle Number	SiO_2	TiO_2	Al_2O_3	FeO	MnO	MgO	CaO	Na_2O	K_2O	P_2O_5	SO_3	Cr_2O_3	NiO	Total	Mg#
44-44.5_1	76.43	0.19	13.30	0.99	0.06	0.10	2.45	3.91	1.78	0.00	0.03	0.01	0.01	99.27	14.99
44-44.5_10	77.63	0.23	13.04	0.38	0.02	0.01	1.47	4.87	2.36	0.00	0.02	0.00	0.01	100.05	6.33
44-44.5_11	75.64	0.24	11.35	2.45	0.12	0.80	1.81	3.41	1.91	0.06	0.00	0.02	0.01	97.83	36.74
44-44.5_12	73.92	0.15	11.66	2.33	0.08	0.24	1.67	4.17	1.89	0.02	0.00	0.03	0.00	96.15	15.42
44-44.5_13	74.85	0.10	11.96	1.59	0.03	0.06	1.39	4.24	1.90	0.02	0.00	0.03	0.00	96.18	5.86
44-44.5_16	74.05	0.14	12.19	2.01	0.06	0.19	1.79	4.21	1.85	0.04	0.00	0.01	0.00	96.54	14.70
44-44.5_17	65.49	0.37	15.16	4.55	0.20	2.33	7.11	4.29	0.27	0.08	0.05	0.03	0.02	99.94	47.72
44-44.5_18	79.36	0.36	12.78	0.57	0.03	0.06	3.25	4.09	0.31	0.04	0.00	0.01	0.00	100.87	16.82
44-44.5_20	81.77	0.08	11.22	0.26	0.00	0.00	3.07	3.55	0.27	0.02	0.00	0.00	0.00	100.25	0.00
44-44.5_21	76.51	0.13	13.64	1.11	0.05	0.18	2.84	4.77	0.66	0.01	0.00	0.00	0.00	99.88	22.13
44-44.5_22	75.33	0.10	14.03	0.50	0.02	0.03	2.74	5.15	0.68	0.02	0.00	0.00	0.00	98.60	8.51

Table 14 Cryptotephra glass major element composition as determined by EMPA for Interval 44.5-45cm

Particle Number	SiO_2	TiO_2	Al_2O_3	FeO	MnO	MgO	CaO	Na_2O	K_2O	P_2O_5	SO_3	Cr_2O_3	NiO	Total	Mg#
44.5-45_1	74.59	0.18	8.78	0.70	0.00	0.03	1.43	1.90	2.49	0.00	0.04	0.00	0.00	90.14	6.44
44.5-45_2	86.82	0.08	8.19	0.17	0.01	0.00	1.89	2.45	0.74	0.00	0.01	0.00	0.00	100.35	0.00
44.5-45_3	72.73	0.50	13.29	3.54	0.11	0.51	2.26	5.86	0.69	0.13	0.04	0.03	0.04	99.74	20.46
44.5-45_4	75.27	0.45	12.76	1.86	0.05	0.28	2.16	5.32	0.62	0.05	0.00	0.00	0.00	98.82	21.25
44.5-45_5	73.62	0.14	13.10	1.28	0.06	0.11	1.72	4.52	2.47	0.00	0.01	0.00	0.00	97.03	13.03
44.5-45_6	70.72	0.07	18.17	0.68	0.02	0.04	5.86	4.89	0.30	0.02	0.05	0.00	0.00	100.82	9.98
44.5-45_7	74.58	0.10	12.04	2.05	0.10	0.24	1.73	4.21	1.88	0.02	0.03	0.00	0.00	96.98	17.09
44.5-45_8	74.53	0.16	12.15	1.68	0.06	0.12	1.63	4.24	1.99	0.03	0.02	0.00	0.00	96.61	11.39
44.5-45_9	74.39	0.15	12.09	1.63	0.06	0.09	1.54	4.12	1.95	0.00	0.02	0.00	0.00	96.05	9.28
44.5-45_10	75.06	0.13	12.04	1.42	0.03	0.06	1.49	3.96	2.19	0.02	0.03	0.00	0.00	96.44	7.19
44.5-45_11	74.92	0.14	11.99	1.39	0.06	0.07	1.47	4.15	2.17	0.01	0.02	0.00	0.00	96.39	8.59
44.5-45_12	75.17	0.12	11.96	1.39	0.05	0.09	1.46	4.10	2.29	0.00	0.03	0.00	0.00	96.66	10.06
44.5-45_13	75.68	0.17	11.58	1.51	0.08	0.09	1.45	4.17	2.07	0.01	0.02	0.00	0.00	96.84	9.78
44.5-45_14	74.22	0.61	12.90	3.68	0.09	0.57	2.91	3.89	1.66	0.15	0.03	0.00	0.00	100.70	21.54
44.5-45_15	73.99	0.65	13.05	3.66	0.07	0.47	2.90	3.74	2.03	0.10	0.05	0.00	0.00	100.71	18.47
44.5-45_16	73.91	0.41	13.68	2.48	0.07	0.39	3.00	3.95	1.88	0.08	0.06	0.00	0.01	99.92	21.70
44.5-45_17	75.17	0.54	12.90	3.19	0.09	0.44	3.18	4.23	0.91	0.12	0.01	0.00	0.00	100.77	19.78
44.5-45_21	73.76	0.13	11.72	2.33	0.13	0.27	1.92	4.16	1.78	0.03	0.02	0.00	0.00	96.24	17.08
44.5-45_22	75.22	0.13	11.95	1.39	0.08	0.04	1.32	4.32	1.91	0.00	0.00	0.00	0.00	96.37	4.90
44.5-45_24	75.76	0.20	12.22	1.20	0.09	0.15	2.00	3.72	1.70	0.07	0.00	0.01	0.00	97.13	18.34
44.5-45_25	74.59	0.17	12.39	1.32	0.09	0.15	1.96	3.65	1.97	0.03	0.00	0.00	0.00	96.32	16.91

8.3 Appendix C: Trace Element Data (SIMS)

Table 1 Mean ratio of cycles

	Mean ratio of cycles																
Sample	**88Sr/30Si**	**89Y/30Si**	**138Ba/30Si**	**139La/30Si**	**140Ce/30Si**	**141Pr/30Si**	**143Nd/30Si**	**147Sm/30Si**	**151Eu/30Si**	**157Gd/30Si**	**159Tb/30Si**	**163Dy/30Si**	**165Ho/30Si**	**167Er/30Si**	**169Tm/30Si**	**174Yb/30Si**	**175Lu/30Si**
42-42.5_2@15	0.006	0.000	0.003	0.000	0.000	0.000	0.000	0.000	0.000	0.000	0.000	0.000	0.000	0.000	0.000	0.000	0.000
42-42.5_1@16	0.015	0.002	0.002	0.000	0.000	0.000	0.000	0.000	0.000	0.000	0.000	0.000	0.000	0.000	0.000	0.000	0.000
42-42.5_3@18	0.005	0.002	0.005	0.000	0.001	0.000	0.000	0.000	0.000	0.000	0.000	0.000	0.000	0.000	0.000	0.000	0.000
42-42.5_4@19	0.020	0.001	0.004	0.000	0.000	0.000	0.000	0.000	0.000	0.000	0.000	0.000	0.000	0.000	0.000	0.000	0.000
13.5-14_1@20	0.013	0.002	0.001	0.000	0.000	0.000	0.000	0.000	0.000	0.000	0.000	0.000	0.000	0.000	0.000	0.000	0.000
13.5-14_2@21	0.005	0.002	0.004	0.000	0.001	0.000	0.000	0.000	0.000	0.000	0.000	0.000	0.000	0.000	0.000	0.000	0.000
13.5-14_3@22	0.023	0.000	0.002	0.000	0.000	0.000	0.000	0.000	0.000	0.000	0.000	0.000	0.000	0.000	0.000	0.000	0.000
13.5-14_4@24	0.009	0.003	0.003	0.000	0.001	0.000	0.000	0.000	0.000	0.000	0.000	0.000	0.000	0.000	0.000	0.000	0.000
14.5-15_3@25	0.019	0.000	0.001	0.000	0.000	0.000	0.000	0.000	0.000	0.000	0.000	0.000	0.000	0.000	0.000	0.000	0.000
14.5-15_2@26	0.025	0.000	0.001	0.000	0.000	0.000	0.000	0.000	0.000	0.000	0.000	0.000	0.000	0.000	0.000	0.000	0.000
14.5-15_1@27	0.012	0.002	0.002	0.000	0.001	0.000	0.000	0.000	0.000	0.000	0.000	0.000	0.000	0.000	0.000	0.000	0.000
14.5-15_4@28	0.001	0.000	0.007	0.000	0.000	0.000	0.000	0.000	0.000	0.000	0.000	0.000	0.000	0.000	0.000	0.000	0.000
44.5-45_3@30	0.005	0.002	0.005	0.000	0.001	0.000	0.000	0.000	0.000	0.000	0.000	0.000	0.000	0.000	0.000	0.000	0.000
44.5-45_4@31	0.013	0.002	0.002	0.000	0.001	0.000	0.000	0.000	0.000	0.000	0.000	0.000	0.000	0.000	0.000	0.000	0.000
44.5-45_2@33	0.000	0.001	0.000	0.000	0.000	0.000	0.000	0.000	0.000	0.000	0.000	0.000	0.000	0.000	0.000	0.000	0.000
44.5-45_1@34	0.008	0.003	0.002	0.000	0.000	0.000	0.000	0.000	0.000	0.000	0.000	0.000	0.000	0.000	0.000	0.000	0.000
14.5-15_3@39	0.011	0.004	0.003	0.000	0.001	0.000	0.000	0.000	0.000	0.000	0.000	0.000	0.000	0.000	0.000	0.000	0.000
14.5-15_4@41	0.003	0.001	0.002	0.000	0.000	0.000	0.000	0.000	0.000	0.000	0.000	0.000	0.000	0.000	0.000	0.000	0.000

Table 2 Concentrations with Errors

Sample	Sr	Y	Ba	La	Ce	Pr	Nd	Sm	Eu	Gd	Tb	Dy	Ho	Er	Tm	Yb	Lu
42-42.5_2@15	117.10	1.41	150.28	3.78	6.24	0.65	2.01	0.27	0.44	0.20	0.01	0.10	0.02	0.14	-0.02	0.10	0.04
42-42.5_1@16	296.17	28.83	101.97	6.45	17.15	2.49	12.53	3.85	1.12	5.31	0.77	5.12	1.13	2.87	0.47	3.47	0.51
42-42.5_3@18	93.09	32.94	279.58	12.73	29.21	3.82	16.07	4.19	1.01	5.41	0.76	5.23	1.19	3.03	0.53	3.81	0.58
42-42.5_4@19	407.47	9.42	208.28	3.22	6.45	0.86	4.27	1.81	1.35	1.46	0.27	1.83	0.44	1.70	0.23	1.74	0.22
13.5-14_1@20	278.33	23.45	69.97	3.38	9.60	1.31	6.48	2.25	1.07	2.62	0.49	3.93	0.92	3.01	0.60	4.17	0.61
13.5-14_2@21	99.51	25.83	214.01	11.19	25.63	3.25	13.55	3.20	0.73	3.27	0.49	3.35	0.73	1.87	0.33	2.23	0.40
13.5-14_3@22	467.70	3.25	100.40	1.41	2.46	0.27	1.22	0.28	0.85	0.08	0.07	0.39	0.08	0.16	0.03	0.33	0.05
13.5-14_4@24	185.53	48.94	174.21	12.82	32.28	4.69	22.30	6.61	1.44	8.21	1.34	8.42	1.73	4.58	0.76	5.21	0.76
14.5-15_3@25	393.67	1.39	35.50	0.56	1.12	0.15	0.25	-0.04	0.56	-0.09	0.00	-0.07	-0.02	-0.15	-0.04	-0.10	-0.03
14.5-15_2@26	519.14	1.20	43.33	3.40	5.18	0.66	2.07	0.35	0.70	0.01	0.42	0.05	0.06	0.08	-0.02	-0.03	-0.04
14.5-15_1@27	245.95	29.40	125.63	8.66	22.53	3.35	16.34	5.07	1.26	6.30	1.01	6.87	1.43	3.80	0.56	4.18	0.57
14.5-15_4@28	26.36	5.66	359.69	1.17	2.48	0.40	2.07	0.67	0.54	0.58	0.11	0.82	0.23	0.54	0.07	0.82	0.12
44.5-45_3@30	101.35	23.27	236.30	9.73	22.63	2.91	12.36	3.64	0.75	3.82	0.67	3.97	0.84	2.17	0.40	2.56	0.40
44.5-45_4@31	263.13	24.74	125.45	8.37	20.59	2.84	13.91	3.82	1.07	4.91	0.86	4.93	1.08	2.81	0.48	3.80	0.51
44.5-45_2@33	1.88	8.25	0.79	0.05	0.17	0.04	0.75	0.14	0.02	0.58	0.16	1.37	0.42	1.67	0.33	2.73	0.55
44.5-45_1@34	161.41	33.90	96.61	6.54	18.04	3.00	15.21	5.66	1.22	7.27	1.26	8.92	1.95	5.20	0.92	6.28	1.01
14.5-15_3@39	221.40	51.39	141.40	10.73	28.04	4.44	21.44	7.01	1.53	9.75	1.54	8.50	1.95	5.46	0.74	6.05	0.80
14.5-15_4@41	68.94	8.31	119.32	3.51	6.85	0.89	3.60	7.39	0.33	1.02	0.20	1.24	0.31	1.08	0.14	1.28	0.19
	2 sigma error																
Sample	**Sr**	**Y**	**Ba**	**La**	**Ce**	**Pr**	**Nd**	**Sm**	**Eu**	**Gd**	**Tb**	**Dy**	**Ho**	**Er**	**Tm**	**Yb**	**Lu**
42-42.5_2@15	4.45	0.30	6.68	0.20	0.40	0.06	0.42	0.24	0.03	0.17	0.01	0.07	0.03	0.14	-0.01	0.11	0.07
42-42.5_1@16	12.97	1.15	6.96	0.81	1.55	0.16	1.15	0.85	0.12	1.28	0.15	0.49	0.09	0.41	0.09	0.50	0.10
42-42.5_3@18	3.27	0.96	10.50	0.55	1.09	0.27	0.84	0.72	0.09	0.56	0.05	0.50	0.09	0.34	0.05	0.22	0.04
42-42.5_4@19	13.82	3.74	12.49	0.57	1.54	0.28	1.49	1.20	0.10	0.70	0.12	0.81	0.18	0.60	0.14	1.02	0.14
13.5-14_1@20	10.57	1.82	2.35	0.20	0.46	0.09	0.51	0.51	0.16	0.40	0.04	0.32	0.11	0.33	0.05	0.42	0.05
13.5-14_2@21	3.32	10.12	17.33	3.30	7.72	1.07	3.72	1.16	0.11	1.59	0.12	0.57	0.12	0.32	0.05	0.43	0.10
13.5-14_3@22	16.26	0.39	6.57	0.19	0.51	0.05	0.52	0.26	0.13	0.25	0.05	0.16	0.04	0.18	0.04	0.15	0.04
13.5-14_4@24	10.56	2.21	11.63	0.33	1.12	0.22	1.29	0.98	0.07	0.79	0.13	0.46	0.10	0.66	0.09	0.44	0.10
14.5-15_3@25	17.41	0.14	1.24	0.07	0.12	0.07	0.19	-0.25	0.08	-0.22	-0.04	-0.10	-0.02	-0.13	-0.03	-0.08	-0.03
14.5-15_2@26	16.91	0.11	1.66	0.34	0.36	0.21	0.54	0.17	0.09	0.21	0.76	0.09	0.11	0.17	-0.02	-0.07	-0.08
14.5-15_1@27	12.48	1.42	9.75	1.08	1.98	0.27	1.99	0.94	0.16	1.13	0.13	1.04	0.20	0.67	0.15	0.64	0.08

14.5-15_4@28	2.23	5.36	52.49	0.22	1.13	0.27	1.64	0.66	0.18	0.76	0.12	0.66	0.17	0.58	0.09	0.81	0.14
44.5-45_3@30	3.48	2.09	9.20	0.42	1.15	0.19	0.78	0.62	0.06	0.68	0.09	0.39	0.17	0.25	0.05	0.21	0.08
44.5-45_4@31	8.89	0.84	4.52	0.41	0.68	0.15	1.39	0.75	0.12	0.73	0.07	0.39	0.06	0.40	0.06	0.76	0.08
44.5-45_2@33	0.27	0.33	0.49	0.07	0.06	0.02	1.28	0.21	0.02	0.20	0.04	0.08	0.04	0.28	0.07	0.17	0.07
44.5-45_1@34	5.60	1.49	4.79	0.41	0.46	0.14	1.23	0.94	0.07	0.99	0.16	0.53	0.09	0.78	0.09	0.60	0.15
14.5-15_3@39	9.65	2.23	5.42	0.56	1.60	0.11	0.98	1.55	0.26	1.52	0.13	0.45	0.26	0.64	0.10	0.80	0.10
14.5-15_4@41	4.20	2.54	5.52	0.40	1.28	0.18	1.06	13.11	0.06	0.55	0.10	0.74	0.19	0.41	0.06	0.40	0.08